Monthly Notices of the ROYAL ASTRONOMICAL SOCIETY

MNRAS **540,** 416–432 (2025) https://doi.org/10.1093/mnras/staf630
Advance Access publication 2025 April 18

The low-frequency size distribution of radio sources in the Lockman Hole

F. Sweijen,[1,2★] J. C. S. Pierce,[3] M. J. Hardcastle,[3] J. H. Croston,[4] L. K. Morabito,[1,2] M. Bondi,[5] J. R. Callingham,[6,7] N. Jurlin,[8] I. Prandoni,[5] H. J. A. Röttgering[7] and R. J. van Weeren[7]

[1] *Centre for Extragalactic Astronomy, Department of Physics, Durham University, South Road, Durham DH1 3LE, UK*
[2] *Institute for Computational Cosmology, Department of Physics, Durham University, South Road, Durham DH1 3LE, UK*
[3] *Centre for Astrophysics Research, University of Hertfordshire, College Lane, Hatfield AL10 9AB, UK*
[4] *School of Physical Sciences, The Open University, Walton Hall, Milton Keynes MK7 6AA, UK*
[5] *INAF – Istituto di Radioastronomia, Via Gobetti 101, I-40129 Bologna, Italy*
[6] *ASTRON, Netherlands Institute for Radio Astronomy, Oude Hoogeveensedijk 4, NL-7991 PD Dwingeloo, the Netherlands*
[7] *Leiden Observatory, Leiden University, PO Box 9513, NL-2300 RA Leiden, the Netherlands*
[8] *Department of Astronomy, The University of Texas at Austin, 2515 Speedway, Stop C1400, Austin, TX 78712-1205, USA*

Accepted 2025 April 10. Received 2025 March 30; in original form 2024 September 16

ABSTRACT

Active galactic nuclei (AGNs) can launch powerful jets that can affect the gas properties in their host galaxies and influence their star formation activity. Depending on their powers and lifetimes and the properties of the surrounding medium, these can remain confined within or close to the galaxy at kiloparsec scales, or grow to giant radio galaxies on megaparsec scales. We measure the projected angular extents of a complete sample of 2110 radio sources ($z < 2.5$; $S_{144\,\mathrm{MHz}} > 600\,\mu\mathrm{Jy}$) using $\nu_{\mathrm{obs}} = 144\,\mathrm{MHz}$ images over a 6.6 deg^2 area of the Lockman Hole field from the International LOw Frequency Array (LOFAR) Telescope (ILT) at resolutions of 6, 1.8, and 0.45 arcsec. Using these measurements, we derive the first radio source size distribution at a frequency below 200 MHz and present a power-linear size diagram for the objects. We then focus on the 1205 sources not identified as star-forming galaxies based on spectral energy distribution classifications from previous work. These have linear sizes in the range $\ell = 0.7$ kpc–1 Mpc, radio powers in the range $P_{144\,\mathrm{MHz}} \approx 10^{21}$–$10^{29}\,\mathrm{W\,Hz^{-1}}$, and a linear size distribution in qualitative agreement with that of radio AGNs in the LOFAR Two-metre Sky Survey. While the sample is limited to radio powers $P_{144\,\mathrm{MHz}} \geq 10^{24}\,\mathrm{W\,Hz^{-1}}$ at higher redshifts due to selection effects, such radio AGNs appear to prefer more compact projected lengths $\ell \lesssim 20$ kpc, which could indicate that more short-lived, high accretion activity was present in the Early Universe.

Key words: galaxies: active – galaxies: jets – radio continuum: galaxies.

1 INTRODUCTION

Radio galaxies can span many orders of magnitude in both size and radio luminosity. Their sizes range from compact pc-scale objects (e.g. Kellermann 1978; Bondi et al. 2018; Cotton et al. 2018) to Mpc-long giants (e.g. Dabhade et al. 2020; Oei et al. 2022). Compact objects have a range of classifiers associated with them such as peaked spectrum, compact steep spectrum, compact symmetric object, and medium symmetric object. For an in-depth discussion of such objects we refer the reader to the recent review by O'Dea & Saikia (2021) and references therein. Here, we focus on the findings that compact objects can display double-lobed, jetted or complex disturbed morphologies when studied at higher resolving powers, resulting from possible interaction with a dense interstellar medium, or a dense intracluster medium (tailed radio galaxies). To investigate the nature of these objects, whether they are young sources or frustrated jets imprisoned by the dense environment surrounding them, direct probes of their size and morphology are required. The compact nature of the aforementioned sources demands observations with sub-arcsecond angular resolution or higher to resolve their structures.

The larger end of the scale is occupied by jetted active galactic nuclei (AGNs) whose jets penetrate out into the extragalactic medium and form the fiducial double-lobed morphology of radio-loud AGNs (RL AGNs). Fanaroff & Riley (1974) created the now archetypal 'FR I' and 'FR II' classification scheme based on the intensity distribution of the source. FR I type sources generally have lower luminosities, are brightest close to the host galaxy, and become more diffuse further away from the host galaxy (e.g. 3C 31, Laing et al. 2008). Conversely, FR II type sources are generally luminous AGNs with most of their brightness contained in 'hotspots' (where the jet terminates in the intergalactic medium), with diffuse lobes of lower surface brightness emission in between the hotspots and the host galaxy (e.g. Cygnus A, Carilli et al. 1991). Results from deeper, higher resolution surveys question the rigidity of this division, however, with the discovery that large populations of compact objects that cannot be placed in either category exist (e.g. 'FR 0s', Baldi, Capetti & Giovannini 2015), as well as FR IIs with radio luminosities below their typical values from previous studies (Mingo et al. 2019). Fig. 2 of Hardcastle & Croston (2020) illustrates the various types of radio galaxies and the vast range of sizes and radio powers they exhibit. Surveys that can

★ E-mail: frits.sweijen@durham.ac.uk

probe both the faintest objects and all relevant scales from compact to giants are thus important to gain a complete overview of radio galaxy morphology.

Radio telescopes have an inherently limited angular resolution set by the dish diameter in the case of single-dish telescopes, or the longest baseline for an interferometer. In the early days of radio astronomy, esoteric techniques such as lunar occultations made it possible to measure positions or angular sizes of compact objects to remarkable accuracy. Hazard, Mackey & Shimmins (1963) used this technique to determine the size of 3C 273 and Swarup (1975) derived a relation between the angular size derived from occultations and flux density. Despite this success, they remained cumbersome to use by their nature. It took the construction of large interferometers with widely separated antennas, such as the Westerbork Synthesis Radio Telescope, the Very Large Array (VLA) and Multi-Element Radio Linked Interferometer Network to start pushing towards more routine sample studies and ultimately to move towards analysis in the image domain.

Knowing the angular size distribution of radio sources benefits our understanding of the Universe in multiple ways. In an abstract sense, the size distribution and related relationships, such as between angular size and flux density or redshift, allow one to derive constraints on cosmological models and investigate whether there is intrinsic evolution within the population aside from cosmological effects (e.g. Kellermann 1972; Kapahi 1975; Swarup 1975; Kapahi, Kulkarni & Subrahmanya 1987; Oort 1988). In more direct ways, the size distribution can serve as a proxy for source age (Longair & Riley 1979), lifetime distribution and kinetic jet power (Hardcastle et al. 2019; hereafter H19), or help study source environments (Croston et al. 2019). This in turn provides input for the theoretical modelling of the evolution of the jets and lobes created by AGNs. Modelling this evolution is a complicated task and as such has long been an active field of research, first in setting up the theoretical frameworks (e.g. Longair, Ryle & Scheuer 1973; Blandford & Rees 1974; Scheuer 1974; Kaiser & Alexander 1997) and then, once computational power increased, simulating their evolution numerically (e.g. Hardcastle & Krause 2013; Turner et al. 2018). Other simulations, while including less of the detailed radio source physics, aim to provide a realistic mock representation of the radio sky, such as the *Square Kilometre Array (SKA) Design Study Simulated Skies* (S^3, Wilman et al. 2008) or *Tiered Radio Extragalactic Continuum Simulation* (T-RECS; Bonaldi et al. 2019). Finally, size measurements can be used to test theoretical source size distribution predictions, such as presented by Saxena, Röttgering & Rigby (2017), and help test the unification theory for radio galaxies and radio-loud quasars (e.g. DiPompeo et al. 2013).

With larger samples of resolved radio sources, it has become possible to start thinking about their evolution in more detail. A key diagram for studying this evolution is the so-called 'power-linear size' diagram that compares radio power with projected physical size (e.g. Baldwin 1982; H19). It allows one to infer where a source might be within its life cycle when combined with predictions from models. The modelling of different scenarios of activity from the central black hole, such as a continuous jet versus a single short-lived outburst, will produce different theoretical tracks across this diagram. In order to test such models, it is important to directly measure the size of radio sources to populate this diagram.

High angular resolution observations play an important role in obtaining reliable source size measurements. Early studies based on data taken with an angular resolution of the order of 10 arcsec or more found that the distribution appeared to approach a constant value roughly between 5 arcsec and 10 arcsec (Swarup 1975). Higher resolution observations, however, showed a different trend. Oort (1988) found a decreasing trend of angular size down to $S_{1.4\,\mathrm{GHz}} = 1$ mJy, with their data suggesting that the median angular size will drop below 1 arcsec for $S_{1412\,\mathrm{MHz}} < 1$ mJy ($S_{144\,\mathrm{MHz}} \lesssim 6$ mJy). A drop in size with decreasing flux density is not unexpected, as the dominant population starts to switch towards star-forming galaxies (SFGs) and radio-quiet AGNs (RQ AGNs), which tend to have more compact radio emission than the RL AGNs that dominate at high flux densities. Prominent recent radio surveys such as the *Low Frequency ARray* (LOFAR; van Haarlem et al. 2013) *Two-metre Sky Survey* (LoTSS; Shimwell et al. 2017, 2019, 2022), a deep ($\sim$70 µJy beam^{-1}) 144 MHz survey of the northern hemisphere, map the radio sky with unprecedented combinations of sensitivity, area, and resolution. However, even with its limiting angular resolution of 6 arcsec, over 80 per cent of sources detected in LoTSS remain (close to) unresolved. The new *Very Large Array Sky Survey* (VLASS; Lacy et al. 2020) at 3 GHz pushes the angular resolution envelope by mapping the northern skies at an angular resolution of 2.5 arcsec (Gordon et al. 2021). This allows the true size distribution to be approximated more precisely through deconvolved sizes, compared to the twice lower resolution of LoTSS, for example. Survey images at sub-arcsecond angular resolution (e.g. Sweijen et al. 2022; de Jong et al. 2024) can push the envelope of deconvolved sizes to less than a few tenths of an arcsecond for sources that remain unresolved even at the arcsecond level.

These projects highlight how observations across a wide range of resolutions and radio powers are needed to properly infer the overall size distribution of radio sources. All-sky surveys are needed to sample the largest or brightest sources that are intrinsically rare, with deeper surveys then sampling the fainter end of the population. Interferometers with dense short spacings are required to provide low angular resolution (of the order of tens of arcseconds to an arcminute) and hence the sensitivity to extended structures required to measure the sizes of large diffuse sources. Ignoring exotic diffuse structures, these will consist of large and giant radio galaxies. Intermediate resolutions in the arcsecond range extend the measurements to the more common smaller radio galaxies and objects like QSOs. Finally, observations with sub-arcsecond angular resolution are needed to determine the sizes of sources that are unresolved at lower resolutions, or provide further limitations on their compactness.

Various techniques have been employed to recover information about source structure on scales below that of the restoring beam, such as Gaussian fitting with deconvolution and fitting visibility amplitudes or phases as a function of baseline length, but they come with their own caveats. Accurate deconvolution requires accurate knowledge of the effective point spread function (psf) for the observations.[1] Furthermore, depending on the signal-to-noise ratio of the detection, such fitting will become increasingly uncertain. An ideal angular resolution is thus one that resolves the sources of interest, such that ambiguities from calibration or psf effects are removed, but not so much that sensitivity to diffuse emission is reduced by too much. Practically, this often translates to a desired resolution about an order of magnitude lower than the scale of interest.

In this work, we study the size distribution of low-frequency radio sources in the sub-arcsecond to arcminute range. Section 2 outlines the data used and sample selected from it. Section 3 describes the methods that were employed to measure the sizes of the sources. The

[1] Imperfect calibration and time or bandwidth smearing, for example, will degrade the actual psf away from its theoretical shape.

Table 1. List of symbols used in this work.

Symbol	Meaning
α	Synchrotron spectral index
ν	Frequency
Ω	Solid angle
$\theta_{\rm maj}$	Fitted major axis of the synthesized beam
$\theta_{\rm min}$	Fitted minor axis of the synthesized beam
ψ	Projected angular size of a source
$\sigma_{\rm rms}$	Local root-mean-square noise in the image
ℓ	Projected physical size of a source
I_ν	Specific peak intensity at frequency ν
L_ν	Specific luminosity at frequency ν
S_ν	Specific flux density at frequency ν
z	Redshift

results of this analysis are presented in Section 4. Section 5 discusses the results in the broader context of the literature. Finally, Section 6 summarizes the work and presents our conclusions.

We define the synchrotron spectral index α through $S \propto \nu^\alpha$. A ΛCDM cosmology with $H_0 = 70\ \mathrm{km\,s^{-1}\,Mpc^{-1}}$, $\Omega_{\rm m} = 0.3$, and $\Omega_\Lambda = 0.7$ is assumed. Quantities indicated with a subscript ν refer to 'spectral' or 'specific' quantities. For brevity we omit these in the text, e.g. 'specific intensity' is referred to as simply 'intensity'. Finally, Table 1 summarizes the symbols used throughout this paper.

2 DATA AND SAMPLE SELECTION

With the *International LOFAR Telescope* (ILT), surveys at sub-arcsecond resolution are now becoming possible. The ILT's wide range of baselines between $\sim 10^2$ and 10^6 m make it sensitive to a wide range of spatial scales. A single eight-hour synthesis observation (as is typical) can now routinely provide high-quality images at angular resolutions of 6, 20, and 60 arcsec (e.g. LoTSS). Recent advances in calibration and imaging techniques have enabled high quality images down to angular resolutions of arcsecond (Ye et al. 2024) and sub-arcsecond level (e.g. Sweijen et al. 2022; Morabito et al. 2022b; de Jong et al. 2024). This allows the projected linear sizes of the low-frequency radio population some tens of kiloparsecs or less in size (depending on their redshift) to be measured directly, and stronger upper limits to be placed on sources that remain compact.

One advantage of the ILT over previous studies at higher frequencies is its sensitivity to larger or more diffuse sources due to the dense network of short baselines. For example, VLASS uses the VLA in its B configuration, for which the largest angular scale (LAS) is 58 arcsec at 3 GHz (S band)[2] and in practice has limited sensitivity to structures above 30 arcsec, whereas LoTSS DR2 has an LAS of 1.2° with an inner uv-cut of 100 m (Shimwell et al. 2022). Thus the sizes of structures that would be undetectable even in principle with a high-resolution VLA survey can be measured with the ILT, subject only to surface brightness constraints.

2.1 Radio data

We use ILT data of the Lockman Hole (Lockman, Jahoda & McCammon 1986) region taken at 144 MHz and centred at $\alpha_{\rm J2000} = 10^{\rm h}47^{\rm m}00^{\rm s}$, $\delta_{\rm J2000} = 58°05'00''$. Three images at angular resolutions of 6, 1.8, and 0.45 arcsec were used, which we will refer to as the standard, intermediate, and high resolution images, respectively. The image properties are summarized in Table 2.

Standard resolution imaging The standard resolution image used is a deep image from the LoTSS Deep Fields DR1. It was generated from 80 h of data, with a central rms noise of $\sigma_{\rm rms}^{\rm LoTSS} \approx 23\ \mu\mathrm{Jy\,beam^{-1}}$ (Kondapally et al. 2021; Tasse et al. 2021).

Intermediate resolution imaging Using the calibration solutions from Sweijen et al. (2022), we imaged the field at a lower resolution by applying a taper to the data. The calibration solutions were applied through WSClean's facet functionality. A flux density scaling factor was derived in the same way as described in Sweijen et al. (2022), by doing source detection with PYBDSF (Mohan & Rafferty 2015) and comparing the flux density of high-SNR sources to the standard resolution image. This yielded an image at an angular resolution of 1.8 arcsec × 0.8 arcsec and a central rms noise of 50 μJy beam^{-1}. It covers the central 6.6 deg^2 of the field of view.

High resolution imaging The high resolution image came from a single 8-h observation (LT10_012, L659948; PI: Best) as presented by Sweijen et al. (2022). We use a mosaic that has been convolved to a common restoring beam of 0.45 arcsec × 0.4 arcsec. The rms noise near the centre is $\sigma_{\rm rms}^{\rm ILT} \approx 25\ \mu\mathrm{Jy\,beam^{-1}}$. It covers the central 6.6 deg^2 of the field of view.

2.2 Sample selection

For this study, a flux density limited sample was constructed in order to ensure good completeness. Shimwell et al. (2019) estimate a 95 per cent completeness in LoTSS for point sources[3] with $S_{144\,\rm MHz} > 450\ \mu$Jy and state that the real completeness limit is likely $\sim$1.3 times higher. We therefore adopt a slightly more conservative flux density cut of $S_{144\,\rm MHz} > 600\ \mu$Jy as measured from the standard resolution image. This provides a sample of 2192 sources over the area where high resolution imaging is available. The detection threshold for sources having a peak intensity exceeding five times the local rms noise are 431 $\mu\mathrm{Jy\,beam^{-1}}$ and 251 $\mu\mathrm{Jy\,beam^{-1}}$ for the intermediate and high resolution images, respectively. The noise values were obtained from rms images created by PYBDSF. It can be seen that the intermediate resolution image has a lower completeness.

To construct an AGN-only sample for comparison with the work of H19, two additional cuts were made:

(i) A source classification cut, to eliminate non-AGNs.
(ii) A redshift cut (z<2.5) to improve the reliability of the classifications.

For removal of the SFGs, we use the classification by Best et al. (2023), who classified sources as SFGs, high and low excitation radio galaxies (HERGs and LERGs) and radio quiet AGNs (RQ AGNs) where possible. The sample classifications is summarized in Table 3.

3 METHODS

Radio luminosities were derived in the usual way through

$$\frac{L_{144\,\rm MHz}}{\mathrm{W\,m^{-2}\,Hz^{-1}}} = 4\pi \left(\frac{D_{\rm L}}{\rm m}\right)^2 \frac{S_{144\,\rm MHz}}{\rm Jy}(1+z)^{-(1+\alpha)}\,\frac{10^{26}\ \rm Jy}{\mathrm{W\,m^{-2}\,Hz^{-1}}}, \tag{1}$$

[2] https://science.nrao.edu/facilities/vla/docs/manuals/oss/performance/resolution

[3] A completeness limit for resolved sources is hard due to the wide variety and complexity of resolved source structure versus the simple nature of point sources.

Table 2. Summary of image properties.

Image resolution	Restoring beam	Central rms (μJy beam^{-1})	Beam area (arcsec^2)	$I^{5\sigma}_{\rm lim}$ (μJy arcsec^{-2})
Standard resolution	6 arcsec × 6 arcsec@0°	23	40.79	2.8
Intermediate resolution	1.8 arcsec × 0.84 arcsec@94°	50	1.71	146
High resolution	0.45 arcsec × 0.40 arcsec@0°	25	0.20	625

Table 3. Source classification for the full S>600 μJy sample.

Classification	№ sources	Fraction	№ redshifts available
SFG	905	41 per cent	905
HERG	165	8 per cent	165
LERG	840	38 per cent	840
RQ AGN	160	7 per cent	160
Uncertain	122	6 per cent	40
Total	2192	100 per cent	2110

where $D_{\rm L}$ is the luminosity distance in metres, $S_{\rm 144MHz}$ is the flux density in Jansky at 144 MHz, z is the redshift and α is the synchrotron spectral index. Redshifts were taken from the Deep Fields DR1 catalogue (Duncan et al. 2021; Kondapally et al. 2021), while for the synchrotron spectral index a fixed fiducial value of $\alpha = -0.8$ was assumed (Condon 1992).

Three methods of measuring source sizes were explored: a flood-fill approach; curves of growth; and 2D-Gaussian fitting. All methods were run on the full sample of sources. Later on, with the help of visual inspection, a final selection of the appropriate measurement was made. More details on each of the size measurement methods used is included in the following subsections. Curves of growth were not used in the final analysis, but for comprehensiveness the method is explained briefly in Appendix A. Each source was therefore assigned a size measurement derived from either the flood-fill algorithm or 2D-Gaussian fitting.

3.1 Flood-fill size estimates

Flood-fill sizes were estimated using a flood-fill algorithm, derived from that used by Mingo et al. (2019). First, an intensity threshold was calculated through max($5\sigma_{\rm rms}$, $I_{\rm peak}/50$), where $\sigma_{\rm rms}$ is the root-mean-square noise in the image. Pixels values below this limit are ignored. After this, the major and minor axes of the source as a whole, as determined by PYBDSF, were used to define an elliptical region outside of which source emission is also ignored, so as to exclude potential emission not associated with the source of interest. Pixels surrounding the initial region with flux densities exceeding the threshold defined above are then 'flooded' to define a region deemed to contain source emission, terminating when surrounding pixels no longer meet the threshold. An angular size is then estimated from the maximum (Euclidean) distance between any of the included pixels. Flux densities were calculated from the non-masked pixels following

$$S = \sum_{x,y} I_{x,y}/\Omega_{\rm beam}, \tag{2}$$

where S is the flux density, $I_{\rm x,y}$ is the intensity of the pixel at the location (x, y) in the image and $\Omega_{\rm beam}$ is the restoring beam area, calculated as

$$\Omega_{\rm beam} = \frac{2\pi\theta_{\rm maj}\theta_{\rm min}}{8\ln 2}, \tag{3}$$

where $\theta_{\rm maj}$ and $\theta_{\rm min}$ are the major and minor axes of the restoring beam (see column 4 of Table 2) in radians.

Size measurements for sources for which the image pixel scale approaches a notable fraction of the linear size will suffer from discretisation. For example, the 1.5 arcsec pixels of the LoTSS image implies an inherent uncertainty of at least 1.5 arcsec in the size estimate. This technique is therefore best suited for heavily resolved sources that are significantly extended with respect to the pixel size and whose surface brightness profile is not easily described by a single or multiple Gaussian components.

3.2 Gaussian fitting estimate

With the Gaussian fitting approach, one or more 2D Gaussian profiles were fitted to the emission. For the LoTSS image, fitting was done with PYBDSF (Mohan & Rafferty 2015). One or more Gaussians were fitted to islands of emission identified based on local rms noise thresholds. The resulting size measurement is the full width at half-maximum (FWHM) of the Gaussian in the case of a single-component source. In the case where multiple Gaussians were fitted to a source, the reported axes are derived from moment analyses. Moments will be naturally 'biased'[4] towards bright compact emission, hence the choice of employing a flood fill algorithm for the largest extended sources. For the intermediate and high resolution images, the imfit package from CASA (CASA Team et al. 2022) was used in the place of PYBDSF, in order to have an independent fit for unresolved or barely resolved sources. Cutouts were made around every source and a single Gaussian was fitted to its intensity distribution. This approach is most suited to sources that are relatively compact and thus reasonably approximated by a Gaussian distribution. For the final measurement, the beam-deconvolved sizes were taken. For consistency with the flood-fill algorithm, sizes from Gaussian fitting for compact sources are reported as twice the FWHM of the beam-deconvolved fitted Gaussian ($2 \times \theta^{\rm DC}_{\rm FWHM}$), approximately equivalent to the width containing emission above $5\sigma_{\rm rms}$, plus two times the fitting uncertainty from PYBDSF.

3.3 Resampling of sources without reliable higher resolution fits

Sources that are in the 6 arcsec sample, but that could not (reliably) be detected or measured at higher resolutions are re-distributed over the bins using a random resampling. One group of sources that was resampled are the ones for which we did not find a reliable measurement at intermediate or high resolution. Another group comes from the caveat that the visual inspection is will have missed the fact that emission can have fallen below the surface brightness limit, leaving a seemingly compact source, but with a reduced peak intensity at higher resolution compared to lower resolution. At a single resolution this is reflected in the ratio between the measured peak intensity and flux density. This would be unity for a true point source. To take into account sources that become resolved by going from 6 to 0.45 arcsec, we apply a flux density ratio threshold of

[4]It is not a true bias, in the sense that the moment is by definition an intensity-weighted proxy.

$S_{0.45\,\mathrm{arcsec}}/S_{6\,\mathrm{arcsec}} < 0.7$, below which sources are considered to be resolved. This factor is an estimate based on the combined uncertainty in the flux density scale, 30 per cent, and the average uncertainty in the fitted flux densities from CASA's `imfit` task for these sources, $\sim$10 per cent, added in quadrature. After applying this threshold, an additional 284 sources were considered resolved and included in the random draws.

In this way we statistically incorporate the information that these failed fits provide. One size boundary of this down-scattering process is set by surface brightness limits in the intermediate resolution image. The limiting surface brightness was estimated as follows. First the surface area of the restoring beam is calculated using equation (3). Using the rms island noise σ_{rms} from PYBDSF as a proxy for the limiting surface brightness per beam, we then estimate the $5\sigma_{\mathrm{rms}}$ surface brightness limit after which we no longer consider the source detectable as

$$I_{\mathrm{lim}}^{5\sigma}\ [\mathrm{Jy\ arcsec^{-2}}] = \left(\frac{5\sigma_{\mathrm{rms}}}{\mathrm{Jy\ beam^{-1}}}\right)\left(\frac{\Omega_{\mathrm{beam}}}{\mathrm{arcsec^2\ beam^{-1}}}\right)^{-1}. \quad (4)$$

By demanding that $I_{\mathrm{lim}} \geq \frac{S}{\Omega_{\mathrm{max}}}$ and assuming a circular source such that $\Omega_{\mathrm{max}} = \theta_{\mathrm{max}}^2$, we obtain an estimated lower limit on this size of

$$\theta_{\mathrm{max}}^{\mathrm{SB}} \geq \sqrt{\frac{8\ln 2}{2\pi}\frac{S_{\mathrm{LoTSS}}}{I_{\mathrm{lim}}^{5\sigma}}}, \quad (5)$$

where S_{LoTSS} is the LoTSS flux density in units of Jy, I_{lim} has units of Jy arcsec^{-2} and $\theta_{\mathrm{max}}^{\mathrm{SB}}$ has units of arcsec. A diffuse source larger than this would fall below the defined surface brightness limit and not be detected. The upper bound is set by twice the deconvolved (DC) size estimate from LoTSS plus three times the uncertainty from PYBDSF's fit: $2(\theta_{\mathrm{LoTSS}}^{\mathrm{DC}} + 3 * \sigma_{\mathrm{maj}})$. New sizes were drawn from a loguniform distribution between these limits, resulting in a random size of

$$\theta_{\mathrm{draw}} = \exp\left\{U\left(\ln\theta_{\mathrm{max}}^{\mathrm{SB}}, \ln\left(2\left(\theta_{\mathrm{LoTSS}}^{\mathrm{DC}} + 3\sigma_{\mathrm{maj}}\right)\right)\right)\right\}, \quad (6)$$

where U indicates a uniform distribution and the factor 2 comes from the way we defined the size of a Gaussian source. The random drawing process was repeated 1000 times to determine the scatter in the resultant size distribution, as shown in Fig. 1. For the results presented in the following section, an arbitrary realization of the drawn sizes was chosen.

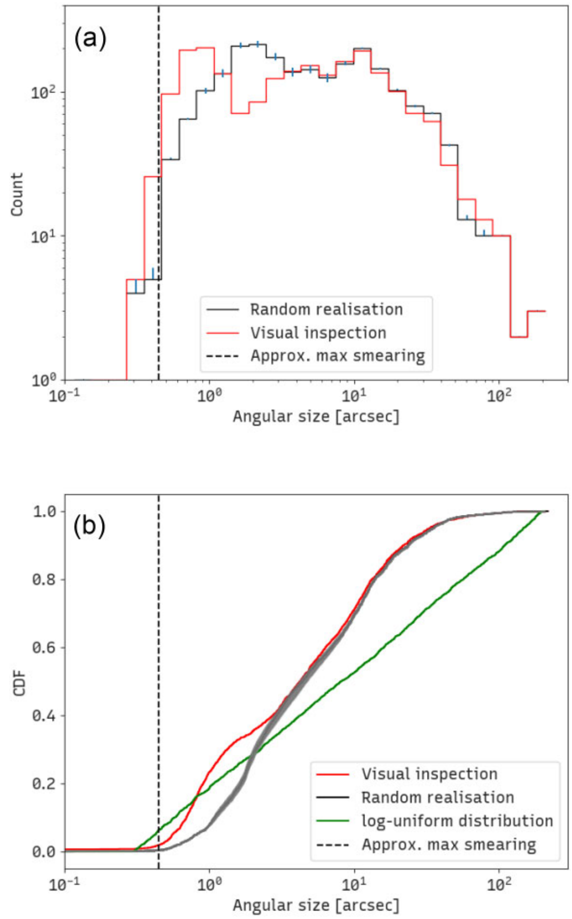

Figure 1. *Panel a:* distribution of measured angular sizes for the full S_{LoTSS}>600 μJy sample. The histogram in red, with a dip in the 2-4" range, indicates the initial measurements after the visual inspection. The black histogram is a random realization from the resampling process, filling the dip. *Panel b:* cumulative distribution functions of the initial measurements after the visual inspection, random realizations and a loguniform distribution (the straight diagonal line) from which random samples were drawn. The grey lines indicate 1000 random realizations. The vertical dashed line indicates the approximate maximum smearing at the edge of the high-resolution image after deconvolving the theoretical psf.

3.4 Visual inspection and cross-check between methods and resolutions

Visual inspection was conducted by overlaying size estimates from the different fits on the LoTSS and ILT images of the sources and checking which provided the best representation of the projected source size. This was most important for sources close to the resolution limit of the standard-resolution images, where the higher resolutions become important for size measurements. For the intermediate resolution image the Gaussian fits were often rejected due to size overestimation caused by the sidelobes of the psf. Two examples of the comparison plots used for this are shown in Fig. 2. The three panels show the standard, intermediate and high-resolution images, and the applicable fitting parameters. When suitable, the sizes derived from each measurement are overlaid as a circle in the standard-resolution image. In the intermediate and high-resolution images the floodfill size is indicated as a semitransparent overlay instead, as for resolved sources this shape can be more irregular. For moderately resolved sources of simple morphology a Gaussian fit and the floodfill method are in general agreement.

Fig. 3 compares the deconvolved major axes of the Gaussian fits from each of the three images with each other. Sources for which the Gaussian fit using the high-resolution image was preferred show a notable discrepancy with a fit using the intermediate-resolution image of the same source, due to the aforementioned contamination from residual psf sidelobes or a poor detection. Sizes of sources for which the intermediate-resolution fit was deemed acceptable agree reasonably with the high-resolution fits and well with the standard-resolution fits. For the high-resolution fits, their deconvolved sizes agree with those derived from the standard-resolution image. We interpret that size measurements of sources in the intermediate-resolution regime could be slightly biased towards more compact sizes due to the quality of the intermediate-resolution image.

3.5 Recovery of (diffuse) emission

Two systematic effects impact our ability to recover diffuse emission at certain scales. One is the uv-coverage inherently constraining

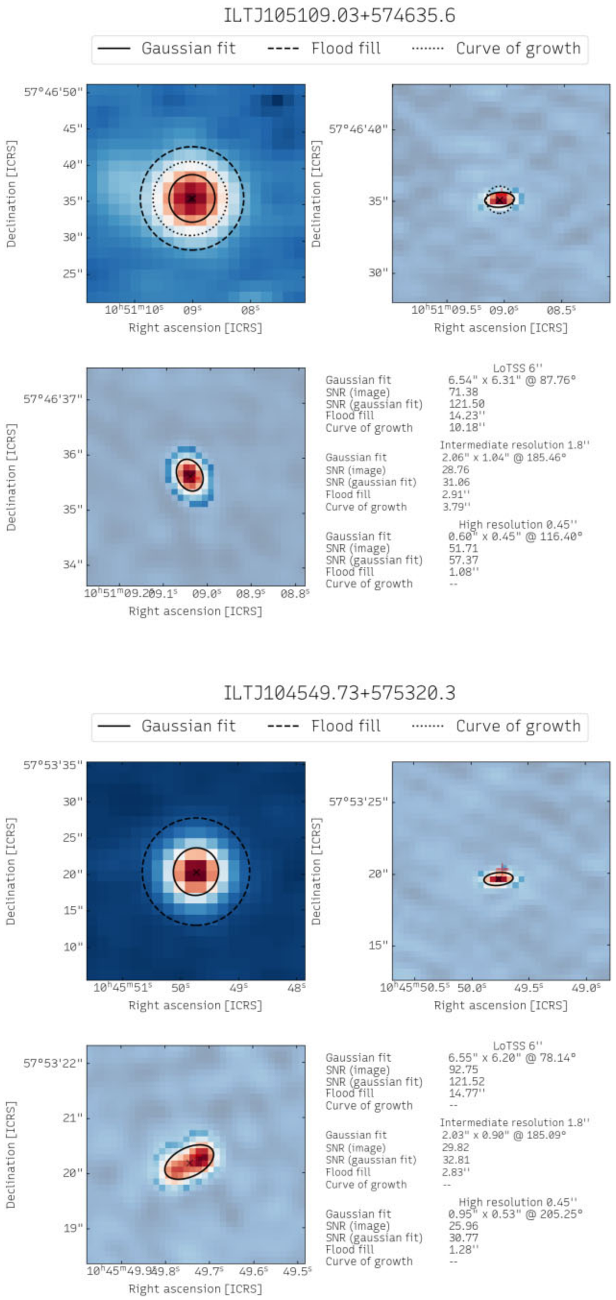

Figure 2. Two examples of the plots used to aid visual inspection. The three images show the source at standard resolution (*top left*), intermediate resolution *(top right*), and high resolution (*bottom left*). Solid black lines indicate the Gaussian fit from PYBDSF (for standard resolution) or imfit for the intermediate and high resolution images. Dotted lines indicate curve-of-growth size if it had converged (not used in the final analysis). Finally, the flood fill sizes are indicated by a dashed line in the standard resolution images or a white semitransparent overlay on the intermediate and high resolution images.

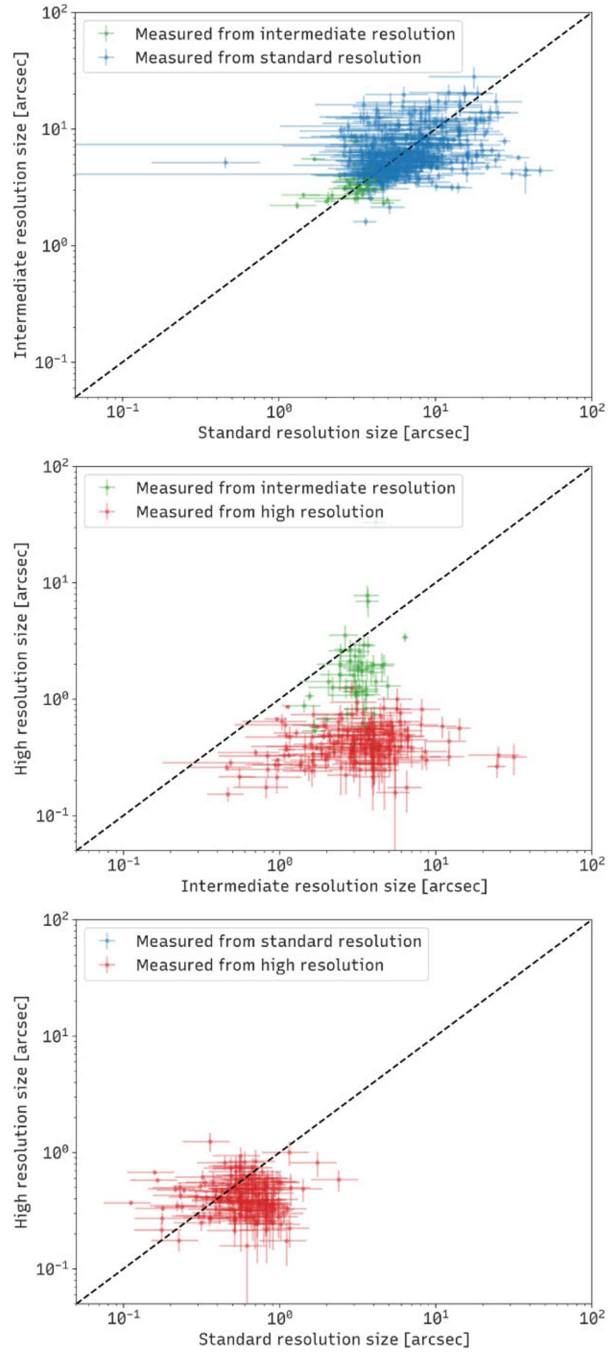

Figure 3. A comparison between the major axis of Gaussian fits at standard, intermediate and high resolution. Error bars indicate uncertainties on the fits reported by PYBDSF or CASA's imfit. Blue points indicate sources for which the standard resolution fit was chose, green points indicate sources for which the intermediate-resolution fit was chosen and red points indicate sources for which the high-resolution fit was chosen. The deviation from the one-to-one line in the middle plot we interpret as the visual inspection preferring high-resolution image in situations where the intermediate-resolution fit was compromised, for example by psf side lobes.

the angular scales that the instrument is sensitive to. The other is the limiting surface brightness at a given resolution. We surmise that combined with the bias towards clearly detected compact objects in the visual inspection process, it is these limitations that contribute to, or drive, the observed dip in the angular size distribution.

3.5.1 *uv-coverage and sensitivity to angular scales*

Where and how well the uv-plane is sampled dictates the angular scales that the instrument is sensitive to. Gaps in the uv-coverage therefore impact the instrument's ability to recover structures on

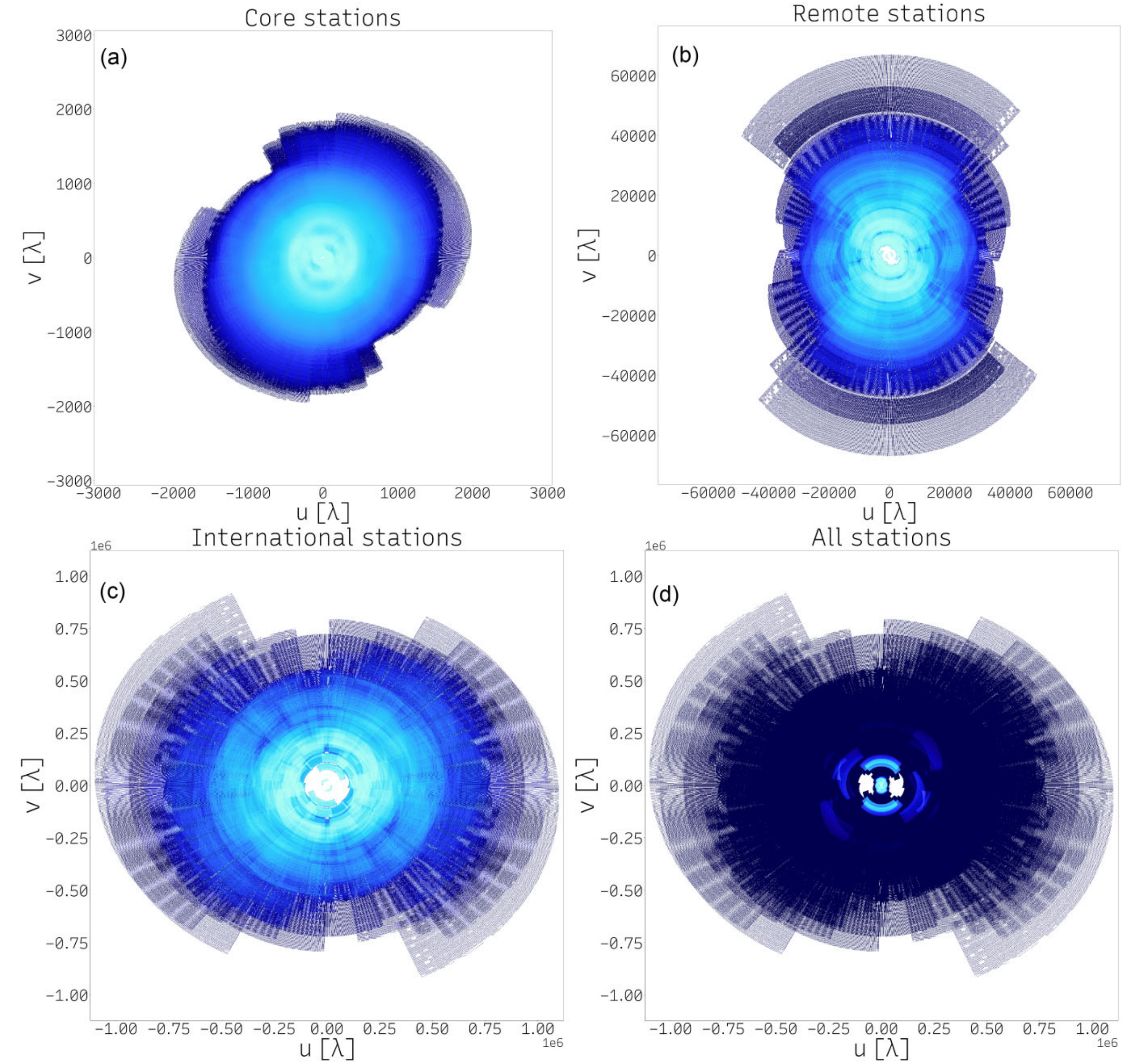

Figure 4. Stokes I uv-coverage of the observation used in this work. The panels show the coverage of core stations only (a), remote stations only (b), international stations only (c), and the full ILT (d). The axes show the v and u coordinates in units of wavelength. A brighter colour indicates a higher relative density of points. Panels are not on the same colour scale to enhance the density contrast in each individual panel.

certain angular scales. Fig. 4 shows the Stokes I uv-coverage of the observation used in this work. The first three panels illustrate how the core, remote and international stations contribute to the uv-coverage separately. Approximately, core stations sample the 80–3000 λ range, remote stations the 3000–50 000 λ range and international stations mostly the 100 000–900 000 λ range (with some extensions inwards to the 50 000–100 000 λ range). The last panel shows the complete uv-coverage of all stations. Despite the ILT's dense sampling of the uv plane, a notable gap in the east–west direction remains. Fig. 5 provides a zoom-in of this gap. It can be seen that, in the east–west direction, the (approximately) 40–100 kλ range lacks sampling. This uv range corresponds to angular resolutions between 2 and 5 arcsec. In the north–south direction a sparsely sampled area around 175 kλ, corresponding to an angular scale of 1.2 arcsec is identified. While not devoid of any sampling, this sparser sampling of the uv-plane in the 1–5 arcsec range will have influenced our ability to recover emission at these scales. We suppose that this has resulted in the diagonal valley separating groups of sources at around $\ell = 10$ kpc in Fig. 6, as such a valley can result from fixed sensitivity to objects of a constant angular size. Ideally, an additional station would provide more intermediate east–west baselines to fill the remaining gap in the uv coverage.

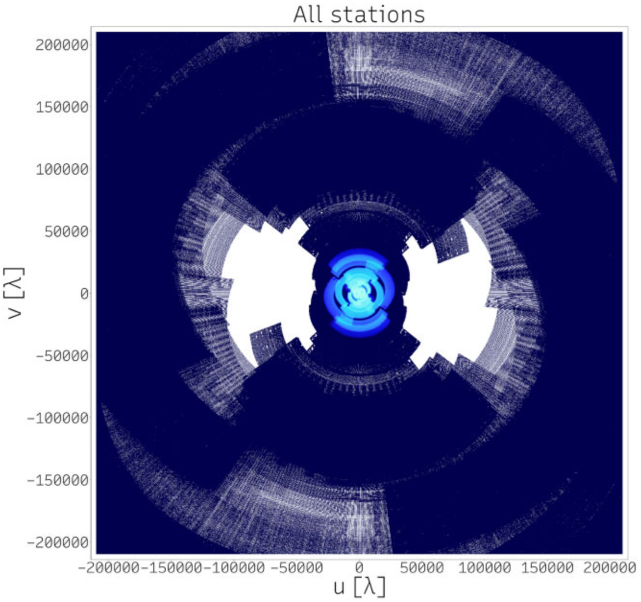

Figure 5. A zoom-in on the inner region of the bottom right panel in Fig. 4 showing the gap in uv-coverage in the (approximately) 40–100 kλ range and the relatively sparse sampling around 175 kλ.

3.6 Definitions of size

The above mentioned limitations lead to a more philosophical consideration of what constitutes 'the size' of a radio galaxy, also discussed in Oei et al. (2023). We also briefly touch on this here. First, a common threshold for source detection is to only consider emission that is brighter than the local (rms) noise level $\sigma_{\rm rms}$ by some factor. This is unavoidable from a reliability perspective, but introduces a survey depth bias where diffuse sources like FR Is or SFGs can 'grow' when newer deeper observations are used to measure the same source. This strengthens the cause for methods such as half-light radii, which, assuming a good fit, will be more robust between various survey depths, but one may argue that those do not reflect the 'actual size' of the object. On a similar note, the intensity profiles of any source with a non-zero spectral index will be frequency dependent. Faint emission or that with a steep spectral index may be missed at higher frequencies, but it is more readily detected at lower frequencies. Comparison between literature values is further complicated when different works use different definitions of 'size', and we encourage future workers to consider carefully how their operational definition matches that of others.

4 RESULTS

4.1 Angular length distribution and flux density versus angular size

Fig. 1 shows the projected angular length distribution for the sample, both before and after the resampling process described in the previous section. The error bars indicate the scatter in each bin resultant from drawing 1000 random realizations. The resampling process helps interpolate the distribution over the observed gap in the angular size distribution in the range ∼1–4 arcsec, which is discussed in more detail in Section 5. For sources whose size was determined through a Gaussian fit, the size is reported as twice the deconvolved FWHM, plus twice the fitting uncertainty. A small subset of the measurements is summarized in Table B1. The catalogue uses the following indications of where a measurement came from: `2xDC_Maj` for a deconvolved size from PYBDSF; `2xDC_Maj_scatt` for a size derived from the resampling process; `LGZ_Size` for floodfill sizes of sources that were inspected visually as part of the LOFAR Galaxy Zoo[5] citizen science project; `LoTSS_code_size`, `1arc_code_size`, `0p3arc_code_size` for flood fill sizes derived from the standard, intermediate, and high resolution imgae respectively; `imfit_1arc`, `imfit_0p3arc` for deconvolved sizes that were derived using CASA's `imfit` task from, respectively, the intermediate and high resolution images.

The left column of Fig. 6 shows the sample's flux density S versus projected angular length ψ. On each opposing side, the marginal distributions are shown. The rows indicate the full sample, sources with $z < 2.5$ and sources with $z < 2.5$ but not classified as SFGs, respectively. Fig. 7 shows the radio power versus projected length for each individual class of HERG, LERG, RQ AGN, SFG, and uncertain sources. The top two histograms in Fig. 8 show the flux density and angular size distributions in more detail. In S–ψ space sources conglomerate at the fainter flux density levels of milliJansky order. In terms of angular size, a wide range is observed, ranging from ∼0.5–200 arcsec.

4.2 Radio power versus linear size

The right column of Fig. 6 shows the sample's radio power P versus projected proper length ℓ. Since not all sources had a redshift estimate available, the sample size shrank by 82 sources from 2192 to 2110. In P–ℓ space the 2110 sources with redshift estimates spread out over a range of radio powers between $P_{144\,\rm MHz} \sim 10^{21}$ W Hz^{-1} and $\sim 10^{28}$ W Hz^{-1}, with an apparent peak between $P_{144\,\rm MHz} \sim 10^{25}$–$10^{26}$ W Hz^{-1} around a proper projected length of $\ell \sim 9$ kpc. Fig. 7 shows this diagram separated by source classification.

Among the SFGs, a number of high-power sources with $P_{144\,\rm MHz} > 10^{25}$ W Hz^{-1} can be seen. These powers are rather high for such objects (e.g. Gürkan et al. 2018). Best et al. (2023) mention that it becomes difficult to distinguish AGN spectral energy distributions (SEDs) from SFG SEDs above redshifts of 2.5. They caution that AGN classification is incomplete above this redshift. We therefore introduce this redshift cut to our sample, which removes a significant number of the higher power sources above $P_{144\,\rm MHz} \sim 10^{25}$ W Hz^{-1}, as can be seen in the middle right diagram of Fig. 6. Subsequently removing sources that have been classified as SFGs by Best et al. (2023), which are outside the scope of this work, mainly removes less powerful sources below this value, in the $\ell \sim 10$–100 kpc range. A small number of objects classified as SFGs extend beyond 100 kpc (also noted by H19), which are likely misclassified.

4.2.1 *Resolution bias, surface brightness limitations, and smearing*

One of the limiting factors in recovering diffuse emission is the surface brightness sensitivity; a quantity that decreases with increasing angular resolution. The estimated sensitivity limits for a 5$\sigma_{\rm rms}$ detection are summarized in Table 2. This effect not only impacts the recovery of diffuse sources such as SFGs, but also biases the extent to which the diffuse jets of FR I type radio galaxies can be measured, for example. The diffuse lobes of FR II type radio galaxies can also be affected by this, but the overall size estimate is likely to be less affected due to the typically prominent hotspots in this type of source. To (partially) overcome these biases the

[5]https://www.zooniverse.org/projects/chrismrp/radio-galaxy-zoo-lofar

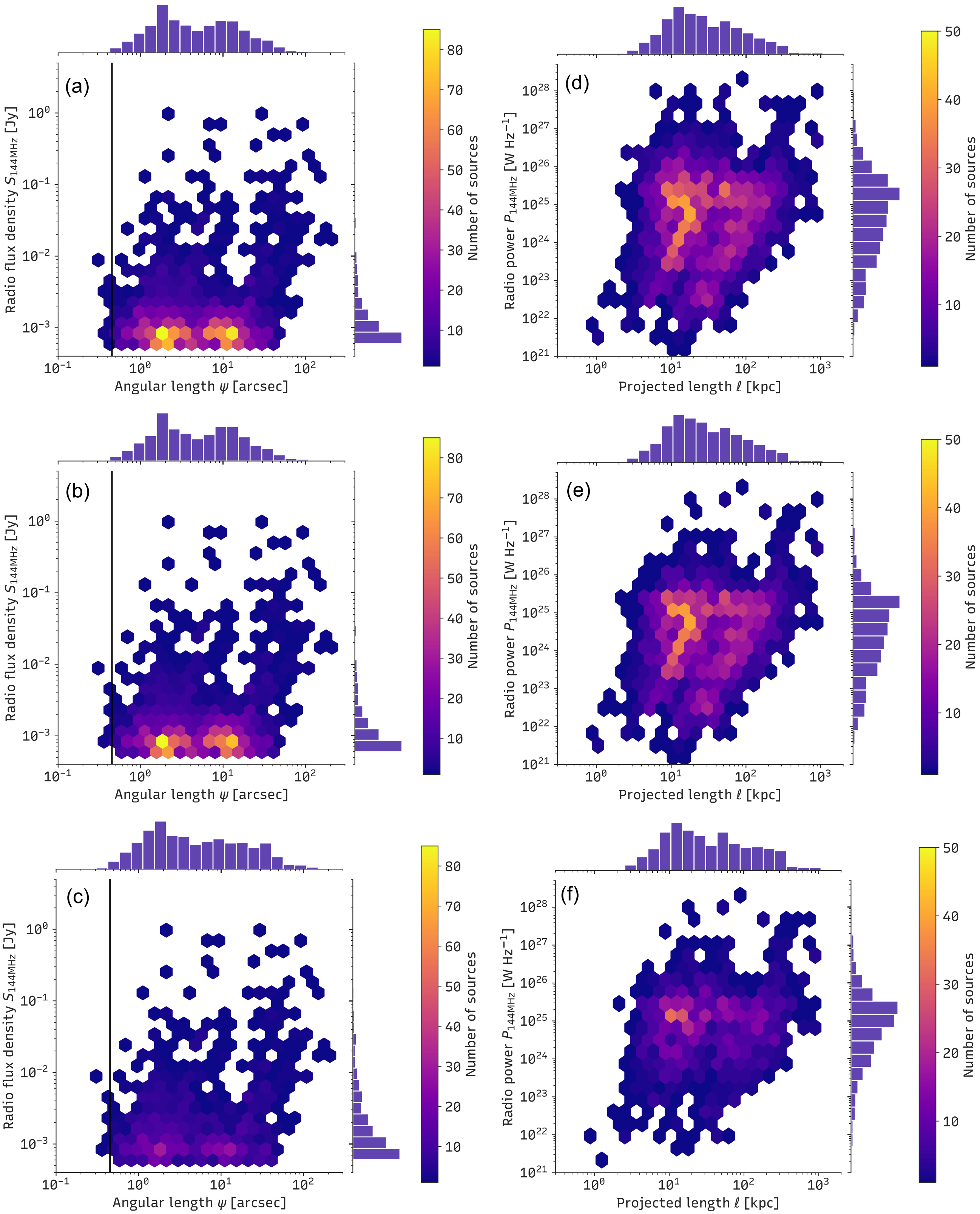

Figure 6. *Left:* flux density versus projected angular length for the full sample (a), sources with z < 2.5 (b) and sources with z < 2.5 excluding those classified as SFGs (c). *Right:* radio power versus projected physical length for the same groups, respectively, in panels d, e, and f.

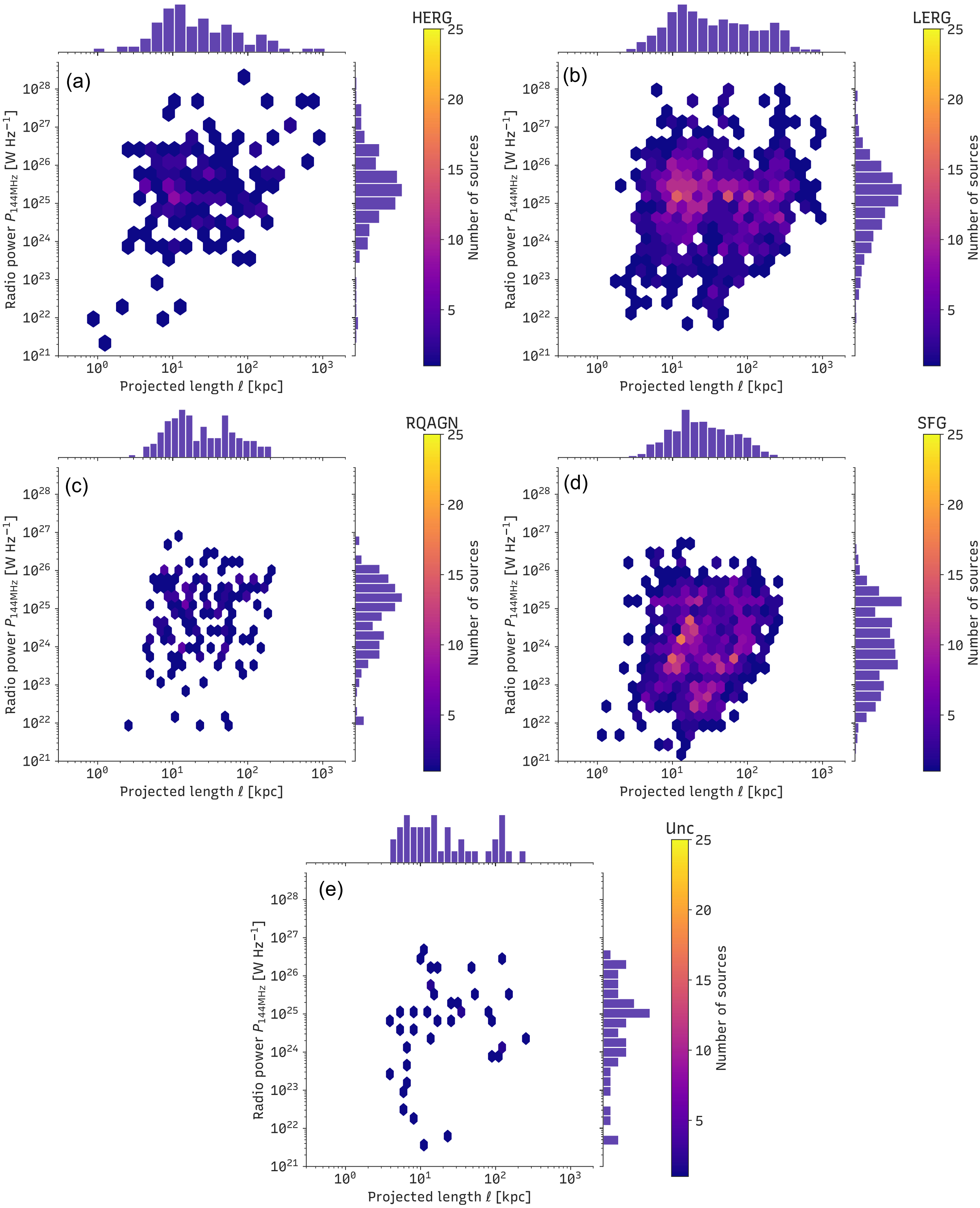

Figure 7. Power versus projected linear size for each source classification: HERGs (a), LERGs (b), RQ AGNs (c), SFGs (d), and unclassified (e).

resampling discussed in Section 3 was used. Another bias related to resolution comes from the visual inspection, where a more compact size would be preferred in the cases where the intermediate resolution fits were rejected, primarily due to the higher noise level and poorer quality in this image. Finally, sources in the high-resolution image will have been affected by time and bandwidth smearing. This will

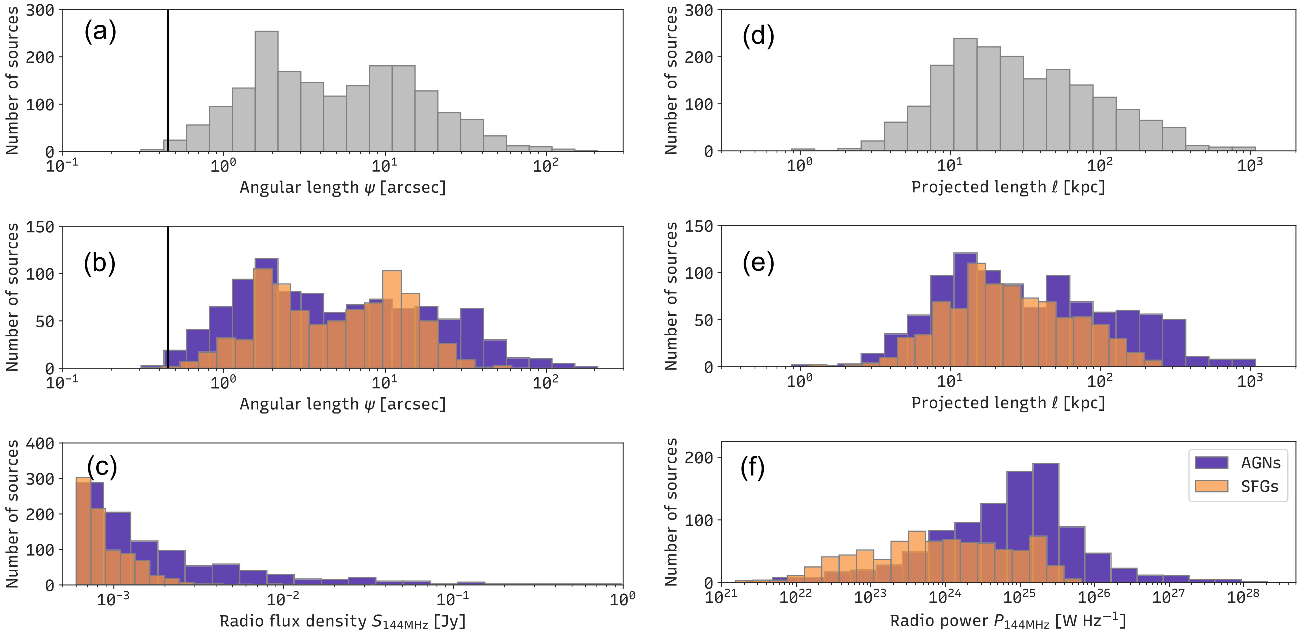

Figure 8. Marginal distributions of Fig. 6. The left histograms show the marginal distributions of the angular length (a, b) and flux density (c) observables for the full sample (a) and separated by AGN or SFG (b, c). The right histograms show the respective derived quantities: physical length (d, e) and power (f) in the same fashion. The black vertical line in panels (a) and (b) indicates the approximate maximum time and bandwidth smearing at the edge of the high-resolution image, after deconvolution with the theoretical psf. Measurements to the left of this line are a combination of upper limits to varying degrees because of smearing effects.

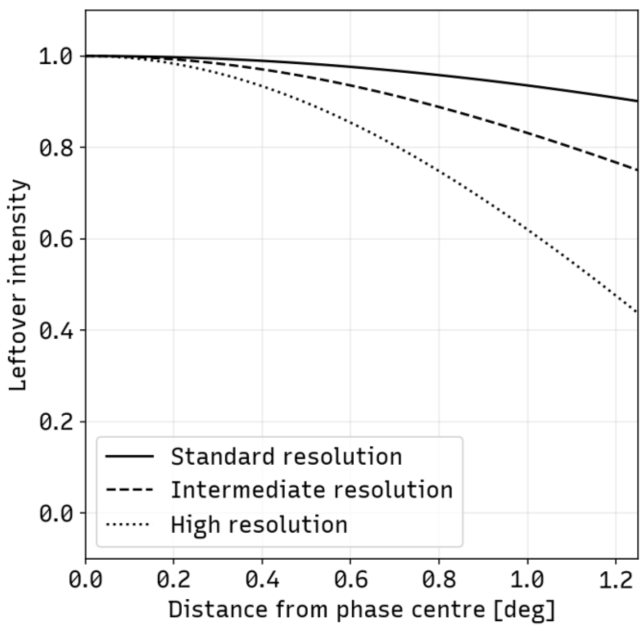

Figure 9. Approximate combined time and bandwidth smearing losses on baselines corresponding to the major axis (i.e. the axis used to measure sizes of Gaussian sources) of the restoring beam of each image. The bandwidth smearing was calculated for 144 MHz; the central frequency of the observation.

have artificially lowered the peak intensity and broadened sources. Using the equations from Bridle & Schwab (1999), the combined smearing losses due to averaging of the data can be estimated. This is summarized in Fig. 9. It can be seen that in the high-resolution image smearing losses can go up to $\sim$51 per cent at the edge of the image at an angular resolution of 0.45 arcsec. Under the assumption that this smearing conserves flux density and affects the major and minor axes equally, the broadening of a Gaussian would be proportional to the square root of the ratio between the unsmeared and smeared peak intensity. A 51 per cent intensity loss then yields a broadening factor for each axis of $\sim$1.4. At the edge of the high-resolution image, point sources are thus smeared to approximately 0.63 arcsec $\times$ 0.56 arcsec at 144 MHz, instead of 0.45 arcsec $\times$ 0.40 arcsec (the common restoring beam of the entire mosaic). This smearing has not been accounted for in the size measurements, as it is intertwined with the issue of selecting genuinely unresolved sources, but will have artificially broadened sources away from the phase centre in a position dependent way. In conclusion, this means that, after deconvolving the common restoring beam, measurements of sources with sizes of $\psi \lesssim 0.44$ arcsec are a complicated mixture of real estimates (if they are close to the phase centre or deconvolved from the lower resolution images) and upper limits.

4.3 Comparison to previous surveys

Fig. 10 presents the median source size measured versus flux density. It is compared against the results from Windhorst et al. (1984, 1990), the T-RECS (Bonaldi et al. 2019), and recent results from LoTSS (H19) and the VLASS Quick Look data (Gordon et al. 2021). Notably, our results agree with the LoTSS results, as would be expected, but show a higher median source size for brighter sources when compared to VLASS. This is discussed in Section 5.1.

5 DISCUSSION

Three regions that are avoided or sparsely inhabited can be identified in the bottom-right P–ℓ diagram presented in Fig. 6. The top and

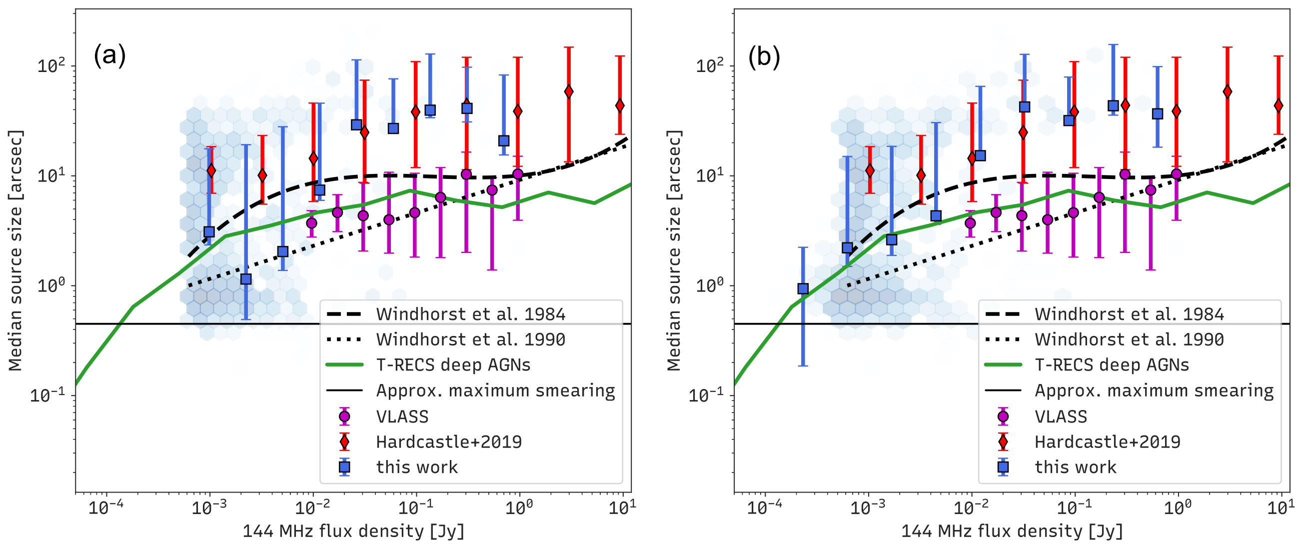

Figure 10. Median source size versus flux density for non-SFG sources, as a function of LoTSS Deep 6’ flux density (a) and as a function of flux density derived from the respective size measurement method (b). Blue squares indicate our work, pink circles indicate VLASS-derived values and the red diamonds indicate values derived from the H19 catalogue. Vertical bars indicate the 16$^{\text{th}}$ and 84$^{\text{th}}$ percentiles within the bin. The dashed black line indicates the empirical relation found by Windhorst, van Heerde & Katgert (1984). The dotted line indicates the relation derived by Windhorst, Mathis & Neuschaefer (1990). The two-dimensional histogram in the background visualizes the distribution used to derive the blue data points. Flux densities were scaled to a 144 MHz value assuming a spectral index of $\alpha = -0.8$. The horizontal black line indicates the approximate maximum time and bandwidth smearing at the edge of the high-resolution image, after deconvolution with the theoretical psf. Measurements below this line are a combination of upper limits to varying degrees due to smearing effects.

top right areas host large, high-power sources. Such sources will be intrinsically rare and require a substantial sky area larger than a single field to be surveyed for large-number statistics. The region in the bottom right corner, to the right of a diagonal line from approximately $(P, \ell) \sim (10^{21}, 30\ \text{kpc})$ to $(P, \ell) \sim (10^{26}, 1000\ \text{kpc})$ is inhabited by large, low-power sources. These will inevitably fall below the surface brightness limit of even low-resolution observations – in this case the 6 arcsec LoTSS data – once they cross a certain limiting surface brightness. Finally, the far left region below lengths of $\ell \sim 3$ kpc is inhabited by the smallest sources, which are either rare because they spend only a fraction of their lives in that regime, are difficult to obtain proper estimates for due to instrumental resolution limitations, or are both small as well as faint, escaping the 600 µJy flux density cut made for our sample.

The plots in Fig. 3 were created to compare the deconvolved sizes between the three angular resolutions. Each of the panels compares deconvolved sizes as measured from the intermediate resolution to the standard resolution, as measured from the high resolution image to the intermediate resolution image and as measured from the high resolution image to the standard resolution image. Overall we conclude that there is no substantial systematic bias between the measurements, except for possibly a small bias towards more compact sizes in the intermediate resolution regime. We expect the quality of these measurements to improve with future reduction of this field that utilise the knowledge gained and strategies developed since Sweijen et al. (2022), as used for the ELAIS-N1 (de Jong et al. 2024) and Böotes (Escott et al., in prep) fields.

5.1 Comparison with literature

In this section, we compare our findings to those of H19. As did H19, we first note the large $\ell > 100$ kpc objects classified as SFGs. These are larger than one would expect for SFGs (e.g. Ward et al. 2024), indicating, for example, possible misclassification or erroneous measurements.

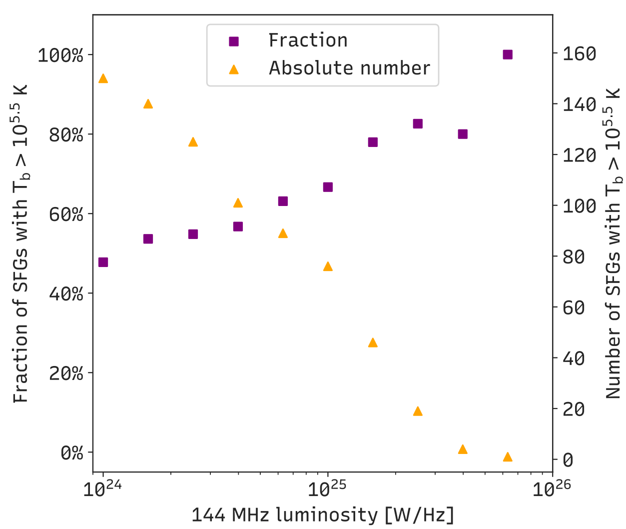

Figure 11. Fraction of objects classified as SFGs that have $L_{144\,\text{MHz}} > 10^{24}\ \text{W Hz}^{-1}$ and a brightness temperature of $T_\text{b} > 10^{5.5}$ K, as measured from a Gaussian fit to the high-resolution image. The left ordinate displays the fraction of sources above a given luminosity exceeding that limit, while the right displays the absolute number of objects.

To investigate these suspicious SFGs and their potential impact on this work we considered two aspects: the brightness temperature of the luminous cases above $L_{144\text{MHz}} > 10^{24}\ \text{W Hz}^{-1}$ (402 sources) and visual inspection of the largest sources with $\ell > 60$ kpc (168 sources). Fig. 11 shows the fraction of sources with $L_{144\,\text{MHz}} > 10^{24}\ \text{W Hz}^{-1}$ that exceed a brightness temperature of $10^{5.5}$ K. This threshold is a reasonable indicator of substantial AGN activity for the ILT (see e.g. Morabito et al. 2022a; Sweijen et al. 2023). It is also expected that the faint radio population is a mixture of SFGs and AGNs (e.g. Morabito et al. 2025). The average flux density ratio between the high and standard resolution image is between 60 and 70 per cent across this luminosity range, which is consistent with this scenario. Including these sources would increase the sample of objects close to the resolution limit by ∼10 per cent, but separating the contributions of the AGN, star formation and potential star-burst activity, and which size to choose for the AGN component would require careful attention beyond the scope of this work. The suspiciously large sources were classified into three broad categories based on visual inspection of PanSTARRS *gri* and BASS *grz* colour composite images: spiral galaxies which visually displayed relatively blue colours and spiral arm-like features, objects with no clear PanSTARRS counterpart or faint or red counterpart in BASS, and complicated systems such as crowded fields, merging galaxies or complex morphologies such as ram-pressure stripping. These categories comprised approximately 36 per cent, 48 per cent, and 15 per cent of the 186 inspected sources, respectively, with the remaining 1 per cent being unclear. Of these, only 7 per cent have spectroscopically confirmed redshifts, while the other 93 per cent are median values from photometric redshift estimates (see Duncan et al. 2021). For the combined 15 per cent of complex objects the large radio size measurements reflect the extent of radio emission, but require more careful interpretation, such as, for example, tails of ram-pressure stripped galaxies. The 48 per cent of the supposedly large SFG sources that have no or no clear counterpart in PanSTARRS could be more distant AGNs (as reasoned similarly by Kondapally et al. 2021 for non-detections in the deep optical data) or dust-obscured objects, as they do generally show WISE counterparts. The 36 per cent that show spiral galaxies as optical counterparts suffer the same problem as the compact AGNs, namely how to define a size of an unresolved or barely resolved objects. Their sizes thus could be overestimated by our definition of $2\times\,\theta^{\mathrm{DC}}_{\mathrm{maj}}$. Summarizing, the tail of luminous or large 'SFGs' are a mixture of genuine SFGs in more complicated scenarios, hybrid objects with both star-formation and a compact AGN component, and possibly distant or dust-obscured AGNs. This means that some of the SFG population is contaminated with AGNs, or vice versa that our sample is incomplete in terms of AGN classification near the resolution limit; however, not in a way that significantly affects the conclusions of this work. Their inclusion would require more detailed inspection of, for example, their SEDs and redshift estimates in order to verify their exact classification.

Fig. 10 plots our measured sizes against the flux density of the source. We compare our findings against those found with the VLASS Quick Look images from Gordon et al. (2021). While an excellent agreement between VLASS and the Windhorst et al. (1990) relation is seen, our median size is notably higher than both VLASS and the T-RECS models for sources with $S \gtrsim 10$ mJy. Two main caveats are at play here, as mentioned by Gordon et al. (2021). First, the configuration used by the VLA prioritises longer baselines. As noted above, the VLASS survey uses the B and BnA configurations, which have a LAS of about 58 arcsec.[6] This reduces the sensitivity to the most extended extended and diffuse sources in our sample. Secondly, the higher angular resolution causes further reduced surface brightness sensitivity and causes extended sources to be resolved into multiple components. Without notable emission connecting the components, source finding algorithms may not consider them as belonging to a single source, causing an underestimate of the true size and introducing spurious small(er) sources. This issue is not unique to VLASS, but is a general source finding and association problem, and part of the reason why for large extended sources we used a different algorithm for our measurements. Visual inspection was carried out for the group of sources with $S \gtrsim 10$ mJy and $\psi > 10$ arcsec comparing the LoTSS 6 arcsec images with the VLASS 2.5 arcsec images. Fig. C1 shows three examples or large, diffuse radio galaxies, confirming that this regime is dominated by objects that form a group of large sources with diffuse emission that is missed by VLASS. Similar discrepancies have been found by e.g. Mandal et al. (2021) and Kondapally et al. (2022) where median sizes derived from LOFAR observations were found to be larger than those derived by Windhorst et al. (1990).

Fig. 10 also compares our results to those of (H19). The main difference between the H19 sample and the sample presented here is that we can now more directly measure sizes of compact sources for which previously only upper limits or deconvolved sizes were available. In their Fig. 8, this corresponds to roughly sources smaller than 20 kpc. A notable difference in our sample is the conglomeration of sources with $\ell = 5$–10 kpc and $P_{144\,\mathrm{MHz}} \sim 10^{25}$–$10^{26}$ W Hz^{-1}. The PD diagram of H19 shows a dearth of sources in this region. One cause can be the difference in redshift coverage. The bulk of that sample resides at $z \lesssim 0.8$, while for this sample we have a notable tail towards (much) higher redshifts. By restricting the sample to sources below this redshift, we recover a distribution of AGNs more similar to H19, as can be seen in Fig. 12. Few sources now lie above $P_{144\,\mathrm{MHz}} \approx 10^{25}$ W Hz^{-1}, except at large projected lengths.

In the bottom panel, the redshift cut is reversed and only sources with $0.8 \le z < 2.5$ are shown. In this redshift range, sources exclusively inhabit the region with estimated radio powers $P_{144\,\mathrm{MHz}} > 10^{24}$ W Hz^{-1}. This exclusiveness is a sensitivity bias from the flux density cut. Despite that, the distributions do imply a tail towards higher radio powers at higher redshifts. If we assume a larger number of high-power radio sources, this may be related to the accretion history of supermassive black holes. The black hole accretion rate density is known to increase towards cosmic noon ($z \sim 2$), matching the cosmic star formation rate density remarkably (Shankar, Weinberg & Miralda-Escudé 2008; Madau & Dickinson 2014). The increase in radio power at higher redshifts could then be attributable to short-lived events at high accretion rates. Another possibility is that these are sources at a younger evolutionary stage that can grow and become more extended at $z < 0.8$.

In terms of sizes, the derived distribution of projected lengths peaks around $\ell = 6$–7 kpc and it appears approximately loguniform for $\ell > 10$ kpc. The peak is likely a resolution effect due to a large number of sources being unresolved at the 6 arcsec resolution of LoTSS and not detected in the ILT images. Even if unresolved, an increase in the number of smaller sources could be indicative of an increasing fraction of younger, smaller sources. However, cosmological surface brightness dimming may affect the detection of larger sources.

6 CONCLUSIONS

In this work, we have measured the size distribution of radio sources in the Lockman Hole area of the LoTSS Deep survey that has ILT coverage. We build on the results from H19 by using images with angular resolutions of 6, 1.8, and 0.45 arcsec, allowing us to probe smaller source sizes. Results for optical counterpart identification in the LOFAR Deep fields also allow us to expand the sample to higher redshifts. We summarize our findings as follows:

[6] https://science.nrao.edu/facilities/vla/docs/manuals/oss2016A/performance/resolution

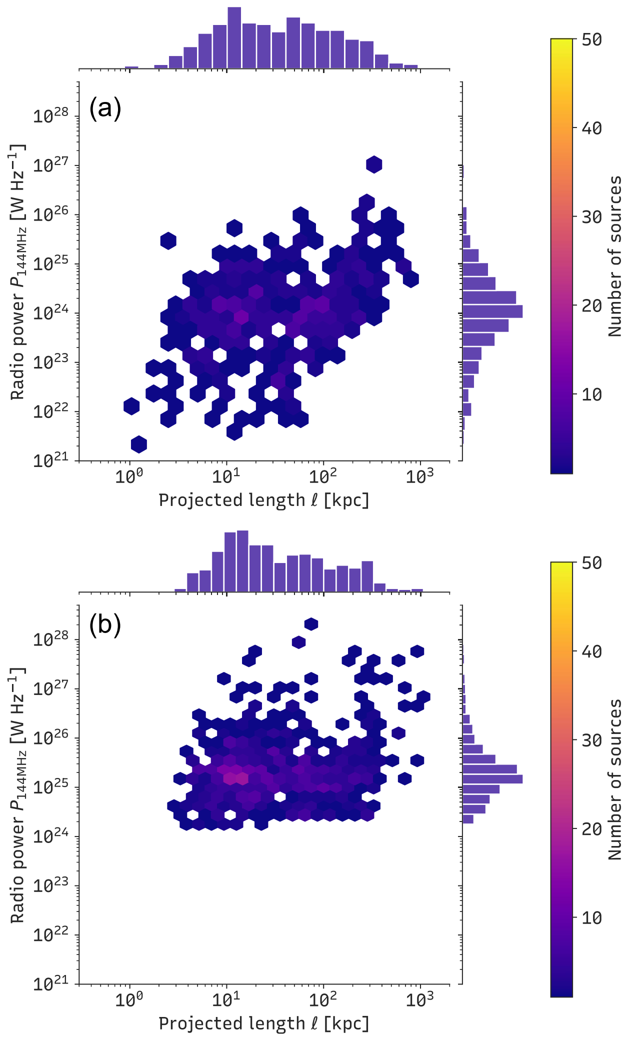

Figure 12. Same as the bottom right figure in Fig. 6 (i.e. no SFGs), except now with a redshift cut of $z < 0.8$ (a) and only sources with redshifts $0.8 \leq z < 2.5$ (b).

(i) We have measured angular sizes between 0.2 and 200 arcsec for radio sources $S_{144\,\mathrm{MHz}} > 600\,\mu$Jy. Physical projected lengths in the range $\ell = 0.7$ kpc–1 Mpc and radio powers in the range $P_{144\,\mathrm{MHz}} \approx 10^{21}$–$5 \times 10^{28}$ W Hz^{-1} were derived using available redshift information from LoTSS Deep DR1.

(ii) We find a significant disagreement between our measurements and previous studies at higher frequencies such as VLASS, which we argue is due to a lack of sensitivity to the extended emission in the high-frequency observations.

(iii) We find a qualitative agreement with the linear size distribution of H19 for sources classified as AGNs by Best et al. (2023) at redshifts $z < 0.8$. At higher redshifts $0.8 \leq z < 2.5$, however, we find a larger number of small sources with radio powers $P_{144\,\mathrm{MHz}} \geq 10^{24}$ W Hz^{-1}. This could imply more short lived high-accretion-rate events in the early Universe.

The ILT's ability to produce science-quality images at both arcsecond and sub-arcsecond scale angular resolutions gives it a unique view on the radio sky, enabling it to detect both compact and diffuse emission from a single observation. Follow-up work will focus on jet power modelling to study the implications of these sizes on AGN life cycles in more detail (Pierce et al., in preparation). Higher resolution observations down to milliarcsecond scales will be required to directly measure sizes of the smallest sources in the sample. Work on the other LOFAR deep fields such as the ELAIS-N1 and Bootes fields will increase the sample size to provide improved statistics in sparsely sampled regions. Finally, with additional stations still joining the array, we highlight the value of additional east–west baselines in the 100–200 km length range, which would be valuable in filling a gap in the ILT's *uv* coverage.

ACKNOWLEDGEMENTS

FS appreciates the support of STFC [ST/Y004159/1]. JCSP and MJH acknowledge support from the UK STFC [ST/V000624/1]. JHC acknowledges support from the UK STFC [ST/X001164/1]. LKM is grateful for support from the Medical Research Council [MR/T042842/1]. MB acknowledges support from INAF under the Large Grant 2022 funding scheme (project 'MeerKAT and LOFAR Team up: a Unique Radio Window on Galaxy/AGN co-Evolution'). IP acknowledges support from INAF under the Large Grant 2022 funding scheme (project 'MeerKAT and LOFAR Team up: a Unique Radio Window on Galaxy/AGN co-Evolution'). RJW acknowledges support from the ERC Starting Grant ClusterWeb 804208. This paper is based (in part) on data obtained with the International LOFAR Telescope (ILT) under project code LT10_012. LOFAR (van Haarlem et al. 2013) is the Low Frequency Array designed and constructed by ASTRON. It has observing, data processing, and data storage facilities in several countries, which are owned by various parties (each with their own funding sources), and which are collectively operated by the ILT foundation under a joint scientific policy. The ILT resources have benefited from the following recent major funding sources: CNRS-INSU, Observatoire de Paris and Université d'Orléans, France; BMBF, MIWF-NRW, MPG, Germany; Science Foundation Ireland (SFI), Department of Business, Enterprise and Innovation (DBEI), Ireland; NWO, The Netherlands; The Science and Technology Facilities Council, UK; Ministry of Science and Higher Education, Poland[7]. This work made use of ASTROPY:[7] a community-developed core PYTHON package and an ecosystem of tools and resources for astronomy (Astropy Collaboration 2013, 2018, 2022). This work made use of NUMPY[8] (Harris et al. 2020).

DATA AVAILABILITY

The data underlying this article and the produced catalogue of size measurements are available at https://lofar-surveys.org/deepfields.html and https://lofar-surveys.org/hdfields.html.

REFERENCES

Astropy Collaboration, 2013, A&A, 558, A33
Astropy Collaboration, 2018, AJ, 156, 123
Astropy Collaboration, 2022, ApJ, 935, 167
Baldi R. D., Capetti A., Giovannini G., 2015, A&A, 576 A38
Baldwin J. E., 1982, in Heeschen D. S., Wade C. M., eds, Extragalactic Radio Sources. International Astronomical Union/Union Astronomique Internationale, Vol. 97, Evolutionary Tracks of Extended Radio Sources. Springer, Dordrecht, p. 21

[7] http://www.astropy.org
[8] https://numpy.org/

Best P. N. et al., 2023, MNRAS, 523, 1729
Blandford R. D., Rees M. J., 1974, MNRAS, 169, 395
Bonaldi A., Bonato M., Galluzzi V., Harrison I., Massardi M., Kay S., De Zotti G., Brown M. L., 2019, MNRAS, 482, 2
Bondi M. et al., 2018, A&A, 618, L8
Bridle A. H., Schwab F. R., 1999, in Taylor G. B., Carilli C. L., Perley R. A., eds, ASP Conf. Ser. Vol. 180, Synthesis Imaging in Radio Astronomy II. Astron. Soc. Pac., San Francisco, p. 371
Carilli C. L., Perley R. A., Dreher J. W., Leahy J. P., 1991, ApJ, 383, 554
CASA Team et al., 2022, PASP, 134, 114501
Condon J. J., 1992, ARA&A, 30, 575
Cotton W. D. et al., 2018, ApJ, 856, 67
Croston J. H. et al., 2019, A&A, 622, A10
Dabhade P. et al., 2020, A&A, 635, A5
de Jong J. M. G. H. J. et al., 2024, A&A, 689, A80
DiPompeo M. A., Runnoe J. C., Myers A. D., Boroson T. A., 2013, ApJ, 774, 24
Duncan K. J. et al., 2021, A&A, 648, A4
Fanaroff B. L., Riley J. M., 1974, MNRAS, 167, 31P
Gordon Y. A. et al., 2021, ApJS, 255, 30
Gürkan G. et al., 2018, MNRAS, 475, 3010
Hardcastle M. J. et al., 2019, A&A, 622, A12 (H19)
Hardcastle M. J., Croston J. H., 2020, New Astron. Rev., 88, 101539
Hardcastle M. J., Krause M. G. H., 2013, MNRAS, 430, 174
Harris C. R. et al., 2020, Nature, 585, 357
Hazard C., Mackey M. B., Shimmins A. J., 1963, Nature, 197, 1037
Kaiser C. R., Alexander P., 1997, MNRAS, 286, 215
Kapahi V. K., 1975, MNRAS, 172, 513
Kapahi V. K., Kulkarni V. K., Subrahmanya C. R., 1987, JA&A, 8, 33
Kellermann K. I., 1972, AJ, 77, 531
Kellermann K. I., 1978, Phys. Scr., 17, 257
Kondapally R. et al., 2021, A&A, 648, A3
Kondapally R. et al., 2022, MNRAS, 513, 3742
Lacy M. et al., 2020, PASP, 132, 035001
Laing R. A., Bridle A. H., Parma P., Feretti L., Giovannini G., Murgia M., Perley R. A., 2008, MNRAS, 386, 657
Lockman F. J., Jahoda K., McCammon D., 1986, ApJ, 302, 432
Longair M. S., Riley J. M., 1979, MNRAS, 188, 625
Longair M. S., Ryle M., Scheuer P. A. G., 1973, MNRAS, 164, 243
Madau P., Dickinson M., 2014, ARA&A, 52, 415
Mandal S. et al., 2021, A&A, 648, A5
Mingo B. et al., 2019, MNRAS, 488, 2701
Mohan N., Rafferty D., 2015, Astrophysics Source Code Library, record ascl:1502.007
Morabito L. K. et al., 2022a, MNRAS, 515, 5758
Morabito L. K. et al., 2022b, A&A, 658, A1
Morabito L. K. et al., 2025, MNRAS, 536, L32
O'Dea C. P., Saikia D. J., 2021, A&AR, 29, 3
Oei M. S. S. L. et al., 2022, A&A, 660, A2
Oei M. S. S. L. et al., 2023, A&A, 672, A163
Oort M. J. A., 1988, A&A, 193, 5
Saxena A., Röttgering H. J. A., Rigby E. E., 2017, MNRAS, 469, 4083
Scheuer P. A. G., 1974, MNRAS, 166, 513
Shankar F., Weinberg D. H., Miralda-Escudé J., 2008, ApJ, 690, 20
Shimwell T. W. et al., 2017, A&A, 598, A104
Shimwell T. W. et al., 2019, A&A, 622, A1
Shimwell T. W. et al., 2022, A&A, 659, A1
Swarup G., 1975, MNRAS, 172, 501
Sweijen F. et al., 2022, Nat. Astron., 6, 350
Sweijen F. et al., 2023, A&A, 671, A85
Tasse C. et al., 2021, A&A, 648, A1
Turner R. J., Rogers J. G., Shabala S. S., Krause M. G. H., 2018, MNRAS, 473, 4179
van Haarlem M. P. et al., 2013, A&A, 556, A2
Ward E. et al., 2024, ApJ, 962, 176
Wilman R. J. et al., 2008, MNRAS, 388, 1335
Windhorst R. A., van Heerde G. M., Katgert P., 1984, A&AS, 58, 1
Windhorst R., Mathis D., Neuschaefer L., 1990, 10, 389
Ye H. et al., 2024, A&A, 691, A347

APPENDIX A: CURVE-OF-GROWTH ESTIMATE

With the curve-of-growth method, a flux-density profile is computed by measuring the enclosed flux density in increasingly large circular apertures. These apertures grow in multiples of the pixel size. By interpolating the resulting curves between the discrete radii, the uncertainty limit imposed by the pixel size can be somewhat overcome, allowing a more precise size to be estimated in theory. A source's size is set to the diameter out to which a certain fraction of a reference flux density is recovered. Such a size is similar to the concept of the half-light radius. It has the potential to allow for the recovery of fainter emission that would normally escape a noise threshold, under the assumption that the reference flux density is close to the true total flux density. Given the high flux density cut of our sample (approximately SNR$>$30 in the LoTSS Deep Field catalogue), we consider it safe to assume that the 6 arcsec flux density is close to the true flux density and thus use that as a reference point.

In practice, however, the curve of growth method was found to be sensitive to artefacts and also to image fidelity. Radio astronomical images are rarely perfect and artefact free. The background noise therefore does not always exhibit uniform behaviour. Additionally, faint diffuse emission close to the noise threshold may not be properly deconvolved. These issues affect both the stability of the curve of growth and the interpretation of what is measured, as the image intensities are expressed in units of the clean restoring beam while underconvolved emission has units of the psf. This makes curve of growth measurements most suited for high-SNR sources, sources that are relatively symmetric in terms of their intensity distribution (to avoid centroiding issues), and artefact free sources. Given these issues and the suitability of the other methods, curves of growth were not used for the final source size measurements.

APPENDIX B: TABLE EXCERPT

Example table entries of a selection of columns from the catalogue produced in this work. The electronic version contains additional columns reporting the uncertainties on the size measurements, but for visual clarity and page size limitations these have been omitted in the text.

Table B1. Example of the table of measurements associated to this work. The full version is available from https://lofar-surveys.org/hdfields.html. The columns are, from left to right, (1) the name of the source in the LoTSS catalogue; (2) right ascension; (3) declination; (4) redshift estimate if available, or −99 otherwise; (5) flux density as measured in LoTSS Deep DR1; (6) 144 MHz luminosity based on the flux density measured from the standard resolution image and the redshift estimate; (7) the size in arcseconds that was chosen as the final measurement; (8) the linear projected size in kpc derived using the available redshift; (9) the method of measurement resulting in the size reported as the final size; (10, 11) the major and minor axes of the Gaussian fit on the standard-resolution image; (12, 13) the major and minor axes of the Gaussian fit on the intermediate-resolution image when available; (14, 15) the major and minor axes of the Gaussian fit on the high-resolution image when available; (16, 17, 18) the size derived using the floodfill algorithm when available; (19, 20) if the size measurement is an upper limit or not and the reason why.

Source name	RA	DEC	z	S_{LoTSS}	$L_{144\,\mathrm{MHz}}$	ψ	ℓ	Method	$\theta^{\mathrm{DC}}_{\mathrm{maj,S}}$	$\theta^{\mathrm{DC}}_{\mathrm{min,S}}$	$\theta^{\mathrm{DC}}_{\mathrm{maj,I}}$	$\theta^{\mathrm{DC}}_{\mathrm{min,I}}$	$\theta^{\mathrm{DC}}_{\mathrm{maj,H}}$	$\theta^{\mathrm{DC}}_{\mathrm{min,H}}$	$\theta_{\mathrm{flood,S}}$	$\theta_{\mathrm{flood,I}}$	$\theta_{\mathrm{flood,H}}$	Upper limit	Upper limit reason
ILTJ103908.15+580420.3	159.78	58.07	2.29	7.99e − 04	2.54e + 25	7.45	61.12	2xDC_Maj_scatt	4.05	1.89	5.17	2.48	0.00	0.00	10.92	–	–	False	–
ILTJ103908.35+581351.1	159.78	58.23	0.07	8.68e − 04	1.11e + 22	22.39	31.06	2xDC_Maj	9.74	4.38	14.45	3.17	4.55	0.48	10.82	–	–	False	–
ILTJ103912.32+581440.9	159.80	58.24	2.09	2.54e − 01	6.54e + 27	2.23	18.56	2xDC_Maj_scatt	38.78	6.93	0.00	0.00	0.64	0.19	56.70	45.17	1.74	False	–
ILTJ103912.44+581644.9	159.80	58.28	0.44	6.82e − 04	4.39e + 23	6.85	38.75	2xDC_Maj_scatt	3.04	0.22	5.95	3.64	0.00	0.00	9.60	–	–	False	–
ILTJ103916.66+580930.2	159.82	58.16	0.19	1.18e − 03	1.19e + 23	1.84	5.87	2xDC_Maj_scatt	0.00	0.00	6.13	2.90	0.00	0.00	12.37	–	–	True	dc_maj_zero
ILTJ103917.05+581336.7	159.82	58.23	1.73	7.55e − 04	1.25e + 25	16.79	142.01	2xDC_Maj	7.37	5.68	7.49	1.91	1.10	0.28	9.60	–	–	False	–
ILTJ103918.46+580359.9	159.83	58.07	5.30	6.11e − 04	1.26e + 26	13.02	79.45	2xDC_Maj	5.74	3.76	5.65	2.74	9.11	0.54	8.75	–	–	False	–
ILTJ103918.86+580148.6	159.83	58.03	0.99	3.41e − 03	1.51e + 25	9.57	76.44	2xDC_Maj	4.67	2.29	10.26	3.48	0.00	0.00	15.66	0.40	–	False	–
ILTJ103920.48+580352.6	159.83	58.06	0.34	1.34e − 03	4.88e + 23	4.63	22.44	2xDC_Maj_scatt	4.47	2.15	4.91	2.64	0.45	0.24	12.82	0.00	0.56	False	–
ILTJ103921.99+575755.2	159.84	57.97	0.74	6.62e − 04	1.45e + 24	1.52	11.07	2xDC_Maj_scatt	0.00	0.00	5.54	1.97	4.35	0.68	9.49	–	–	True	dc_maj_zero
ILTJ103923.89+575216.8	159.85	57.87	0.11	1.85e − 03	6.00e + 22	4.19	8.64	2xDC_Maj_scatt	3.02	1.06	2.43	1.28	0.46	0.27	12.37	2.40	0.67	False	–
ILTJ103924.19+581831.7	159.85	58.31	0.30	7.61e − 04	2.14e + 23	9.15	41.11	2xDC_Maj_scatt	9.34	0.00	4.54	2.84	0.00	0.00	16.22	–	–	False	–
ILTJ103925.99+575804.7	159.86	57.97	0.14	1.88e − 03	9.21e + 22	7.29	17.72	imfit_1arc	4.28	3.31	3.65	2.36	7.73	4.59	14.23	1.60	0.35	False	–
ILTJ103927.17+580934.2	159.86	58.16	1.88	8.46e − 04	1.70e + 25	5.66	47.67	2xDC_Maj_scatt	2.23	1.66	4.96	2.01	0.41	0.16	9.49	–	0.47	False	–
ILTJ103929.43+580516.0	159.87	58.09	5.42	3.04e − 02	6.59e + 27	1.02	6.14	2xDC_Maj_scatt	4.39	3.44	1.12	0.60	0.60	0.32	16.77	4.18	1.43	False	–
ILTJ103930.55+581258.8	159.88	58.22	−99.00	2.96e − 03	–	1.18	–	2xDC_Maj_scatt	2.25	1.52	1.49	1.00	0.37	0.34	13.42	2.83	0.98	False	–
ILTJ103930.94+575154.1	159.88	57.86	1.13	6.16e − 04	3.73e + 24	25.49	209.25	LGZ_Size	–	–	50.16	2.23	2.01	0.10	7.50	–	–	False	–
ILTJ103932.39+582231.7	159.88	58.38	0.30	1.30e − 03	3.47e + 23	18.68	82.47	2xDC_Maj	8.38	0.00	4.04	2.78	0.00	0.00	16.16	–	–	False	–
ILTJ103933.59+582140.1	159.89	58.36	0.07	8.69e − 04	9.68e + 21	18.39	23.99	2xDC_Maj	8.32	5.52	10.98	6.89	0.00	0.00	12.37	–	–	False	–
ILTJ103933.85+580030.2	159.89	58.01	2.15	1.26e − 03	3.45e + 25	4.43	36.74	2xDC_Maj_scatt	2.64	1.94	4.61	3.22	0.33	0.25	11.42	1.20	0.64	False	–
ILTJ103935.66+575907.7	159.90	57.99	0.08	1.25e − 03	1.71e + 22	9.11	13.01	2xDC_Maj	4.32	3.11	6.93	3.74	0.00	0.00	13.42	–	–	False	–
ILTJ103936.71+581743.2	159.90	58.30	1.85	2.09e − 03	4.06e + 25	5.78	48.71	2xDC_Maj_scatt	2.76	1.88	3.00	1.01	0.51	0.27	12.90	2.04	0.94	False	–
ILTJ103937.36+580757.3	159.91	58.13	0.51	1.66e − 03	1.51e + 24	4.12	25.29	2xDC_Maj_scatt	2.84	2.11	9.72	2.21	0.41	0.22	10.82	1.26	0.79	False	–
ILTJ103937.38+575701.4	159.91	57.95	0.71	1.07e − 03	2.18e + 24	1.33	9.57	0p3arc_code_size	0.00	0.00	4.15	3.26	1.75	0.28	12.37	0.40	1.33	True	dc_maj_zero
ILTJ103938.52+575211.4	159.91	57.87	0.10	6.70e − 04	1.73e + 22	1.89	3.54	2xDC_Maj_scatt	0.00	0.00	6.32	2.12	0.00	0.00	8.75	–	–	True	dc_maj_zero
ILTJ103938.52+575602.0	159.91	57.93	0.07	9.17e − 04	1.23e + 22	31.56	44.61	2xDC_Maj	13.76	9.17	0.00	0.00	0.00	0.00	13.42	–	–	False	–
ILTJ103938.64+582111.1	159.91	58.35	0.29	1.47e − 03	3.80e + 23	8.63	37.78	2xDC_Maj	4.13	1.64	6.51	2.95	5.69	3.02	12.82	–	0.49	False	–
ILTJ103940.57+580303.3	159.92	58.05	1.98	6.55e − 04	1.48e + 25	4.85	40.61	2xDC_Maj_scatt	2.96	1.55	7.56	3.70	0.00	0.00	9.12	–	0.00	False	–
ILTJ103940.81+580850.5	159.92	58.15	1.63	6.41e − 04	9.20e + 24	5.15	43.61	2xDC_Maj_scatt	3.07	2.23	28.75	5.32	2.63	0.30	8.49	–	–	False	–
ILTJ103941.33+574847.7	159.92	57.81	0.13	8.46e − 04	3.46e + 22	13.13	29.71	2xDC_Maj	5.68	2.24	16.18	4.93	0.00	0.00	12.82	–	–	False	–
ILTJ103941.63+580239.9	159.92	58.04	2.89	3.98e − 03	2.14e + 26	6.13	47.71	imfit_1arc	7.77	0.92	3.06	1.52	1.42	0.46	22.50	2.91	1.83	False	–
ILTJ103942.65+575224.4	159.93	57.87	2.58	1.01e − 03	4.22e + 25	44.01	352.67	2xDC_Maj	18.76	11.31	0.00	0.00	3.84	0.24	4.24	–	–	False	–
ILTJ103942.76+580616.4	159.93	58.10	0.10	8.72e − 01	2.15e + 25	33.40	61.32	2xDC_Maj_scatt	17.01	5.65	1.90	1.12	8.75	4.13	32.38	21.57	19.95	False	–
ILTJ103945.69+574308.2	159.94	57.72	2.78	9.01e − 04	4.44e + 25	0.90	7.11	imfit_0p3arc	0.00	0.00	3.33	2.74	0.45	0.21	10.82	1.26	0.55	True	dc_maj_zero
ILTJ103949.67+575526.3	159.96	57.92	1.55	7.11e − 04	9.06e + 24	12.11	102.59	2xDC_Maj	5.55	2.57	0.00	0.00	1.81	0.12	11.42	–	–	False	–

APPENDIX C: COMPARISON BETWEEN VLASS AND LOTSS

This figure compares the radio emission from six objects between LoTSS and VLASS. This is to demonstrate how surveys like VLASS miss faint extended emission either due to surface brightness sensitivity limitations or because a lack of baselines resolves out certain spatial scales, emphasized by the lack of contours in Fig. C1.

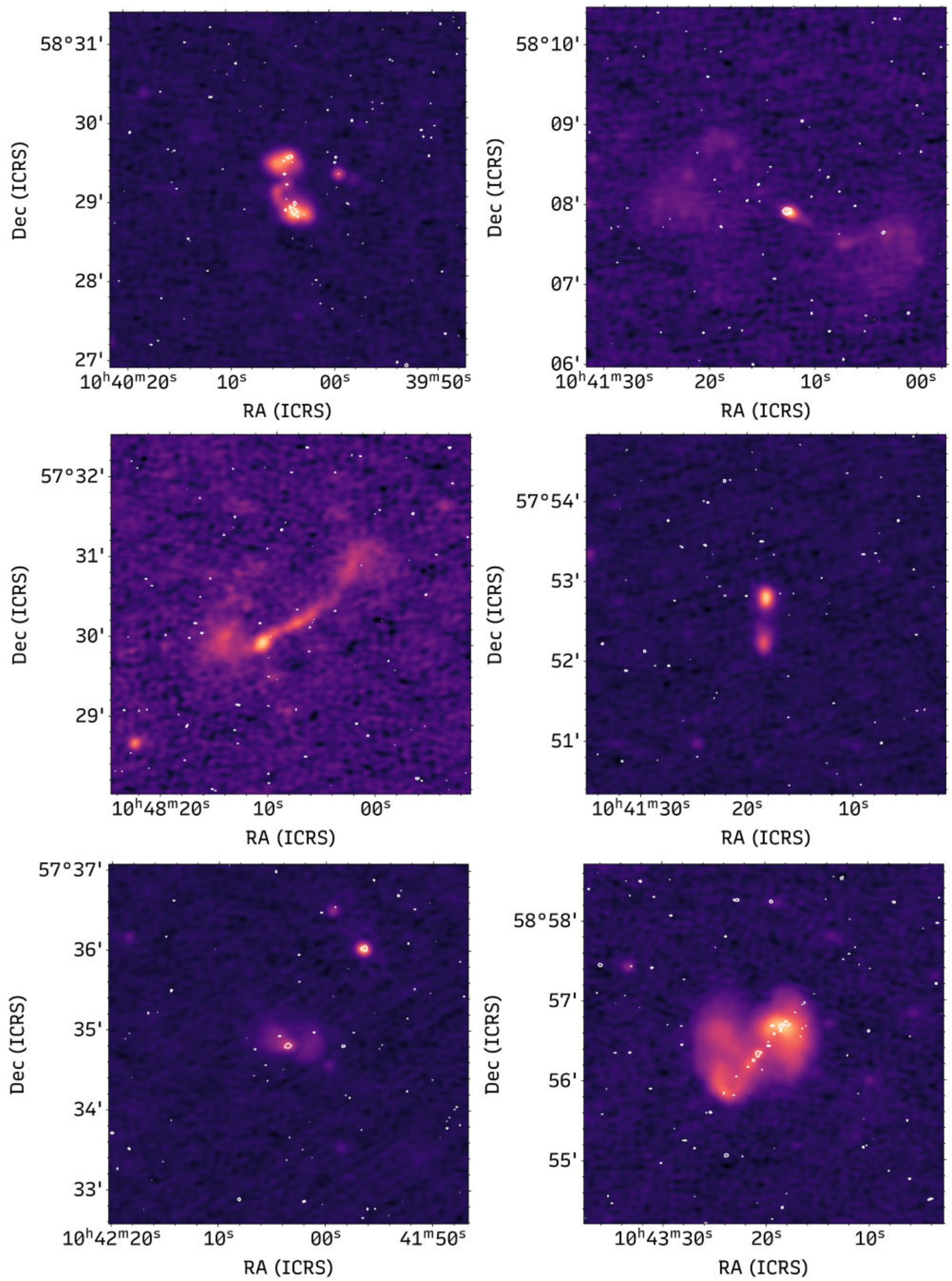

Figure C1. Six examples of the visual inspection of the large ($\psi > 10$ arcsec) and bright ($S > 10$ mJy) sources in Fig. 8. The background image shows the LOTSS 6 arcsec resolution image on a square root stretch, with white contours from VLASS overlaid. Contours are drawn from $3\sigma_{\rm rms}$ up to the 99.9th percentile, in increases of $2\sigma_{\rm rms}\sqrt{2}$.

This paper has been typeset from a TEX/LATEX file prepared by the author.